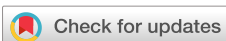


RESEARCH ARTICLE | FEBRUARY 03 2025

From chimeras to extensive chaos in networks of heterogeneous Kuramoto oscillator populations

Pol Floriach  ; Jordi Garcia-Ojalvo  ; Pau Clusella 



Chaos 35, 023115 (2025)

<https://doi.org/10.1063/5.0243379>



View
Online



Export
Citation

Articles You May Be Interested In

Weak chimeras in minimal networks of coupled phase oscillators

Chaos (January 2015)

Heteroclinic switching between chimeras in a ring of six oscillator populations

Chaos (June 2023)

Metastability of multi-population Kuramoto–Sakaguchi oscillators

Chaos (January 2025)

From chimeras to extensive chaos in networks of heterogeneous Kuramoto oscillator populations

Cite as: Chaos 35, 023115 (2025); doi: 10.1063/5.0243379

Submitted: 10 October 2024 · Accepted: 16 January 2025 ·

Published Online: 3 February 2025



View Online



Export Citation



CrossMark

Pol Floriach,¹ Jordi Garcia-Ojalvo,² and Pau Clusella^{3,a}

AFFILIATIONS

¹Department of Mathematical Sciences, University of Copenhagen, Copenhagen DK-2100, Denmark

²Department of Medicine and Life Sciences, Universitat Pompeu Fabra, Barcelona 08003, Spain

³EPSEM, Departament de Matemàtiques, Universitat Politècnica de Catalunya, Manresa 08242, Spain

^aAuthor to whom correspondence should be addressed: pau.clusella@upc.edu

ABSTRACT

Populations of coupled oscillators can exhibit a wide range of complex dynamical behavior, from complete synchronization to chimera and chaotic states. We can, thus, expect complex dynamics to arise in *networks* of such populations. Here, we analyze the dynamics of networks of populations of heterogeneous mean-field coupled Kuramoto–Sakaguchi oscillators and show that the instability that leads to chimera states in a simple two-population model also leads to extensive chaos in large networks of coupled populations. Formally, the system consists of a complex network of oscillator populations whose mesoscopic behavior evolves according to the Ott–Antonsen equations. By considering identical parameters across populations, the system contains a manifold of homogeneous solutions where all populations behave identically. Stability analysis of these homogeneous states provided by the master stability function formalism shows that non-trivial dynamics might emerge on a wide region of the parameter space for arbitrary network topologies. As examples, we first revisit the two-population case and provide a complete bifurcation diagram. Then, we investigate the emergent dynamics in large ring and Erdős–Rényi networks. In both cases, transverse instabilities lead to extensive space–time chaos, i.e., irregular regimes whose complexity scales linearly with the system size. Our work provides a unified analytical framework to understand the emergent dynamics of networks of oscillator populations, from chimera states to robust high-dimensional chaos.

© 2025 Author(s). All article content, except where otherwise noted, is licensed under a Creative Commons Attribution-NonCommercial 4.0 International (CC BY-NC) license (<https://creativecommons.org/licenses/by-nc/4.0/>). <https://doi.org/10.1063/5.0243379>

Many physical systems are composed of large numbers of interacting oscillatory units. Such complex systems typically display synchronization patterns that vary in complexity, depending on the oscillators' intrinsic dynamics and the nature of their interactions. For instance, the Kuramoto–Sakaguchi model provides a simple framework in which a population of globally coupled phase oscillators transitions from incoherence to synchronization as the strength of the coupling is varied. Interestingly, when coupling two populations of Kuramoto–Sakaguchi oscillators other collective dynamics may emerge, in which one population displays a higher degree of synchronization than the other. These regimes are an example of *chimera states*, a phenomena that has been studied in a number of theoretical setups and experimental works. Here, we extend the analysis of these symmetry-breaking transitions to the case of N oscillator populations interacting through arbitrary complex networks. In particular, for ring and random topologies, we reveal the existence of highly chaotic

states whose complexity increases linearly with the system size, a situation known as *extensive chaos*.

I. INTRODUCTION

Chimera states are an intriguing example of non-trivial collective activity emerging in networks of coupled oscillators. In their simple original form, chimera states consist of a population of identical oscillatory units spontaneously splitting into two subgroups: A completely synchronized cluster and a partially synchronized one.^{1,2} This form of spontaneous symmetry breaking was first uncovered in non-locally coupled rings of phase oscillators and has since been studied in a wide variety of theoretical and real systems.^{3,4}

The Kuramoto–Sakaguchi model⁵ provides a simple yet powerful framework to understand the collective behavior of complex oscillatory systems, including chimera states. In this model, each

oscillator corresponds to a single phase variable that interacts with the other units through an all-to-all sinusoidal coupling. Remarkably, this mean-field setup allows an exact low-dimensional reduction through the Ott–Antonsen ansatz.^{6,7} This method provides the collective dynamics of the system as a single differential equation for the complex Kuramoto order parameter.⁸

Researchers have employed the Ott–Antonsen equations to unveil the nature of chimera states in systems composed of two identical populations of Kuramoto–Sakaguchi oscillators.^{9–13} For oscillators with equal natural frequencies, the chimera state always coexists with the homogeneous solution (i.e., full synchronization of the two populations).⁹ However, for oscillators with distributed frequencies, the chimera state might emerge through a pitchfork bifurcation of the homogeneous solution; thus, attracting solutions are always inhomogeneous in wide regions of the parameter space.^{10,12} Interestingly, chimera states are not always stable in these regions, leading to the emergence of other regimes including symmetric oscillations, antiphase states, or even low-dimensional chaos.^{10–14}

A natural question to ask is how do these results translate to large networks of more than two populations. A number of recent studies have addressed this topic^{15–19} (see also Ref. 7 for a thorough review). In particular, Martens^{15,16} studied networks of three populations without disorder and revealed the emergence of different types of chimera states. Lee and Krischer¹⁷ extended these studies and showed the emergence of low-dimensional chaos in the three-population model. The same authors also investigated six populations on a ring topology and showed that chimeras are generally unstable but connected through attracting heteroclinic cycles.¹⁸ On the other hand, Laing¹⁹ investigated the emergence of chimera states in rings composed of different number of populations with non-local coupling. Interestingly, this work shows a chaotic regime appearing through the instability of chimera states. However, this irregular state vanishes as the number of populations in the network increases.

In spite of all this progress, the behavior of identical populations of Kuramoto–Sakaguchi populations interacting through complex networks remains an open problem due to the variety of possible topological configurations. In this paper, we take on this challenge and provide a general unifying framework to study the emergence of spatiotemporal dynamics in these models. We consider networks where the overall external input to each population is normalized across nodes, thus ensuring the existence of homogeneous states. The stability of these trivial regimes to small perturbations can be studied by means of the master stability function,²⁰ which provides the growth rate of arbitrary perturbations as a function of the eigenmodes of the structural connectivity matrix. This method allows one to obtain an analytical expression for the dispersion relation of the homogeneous states.

We show that, for populations with intrinsic disorder, transverse instabilities arise in a wide region of the parameter space for arbitrary network topologies. In the case of two populations, such transverse instability corresponds to the pitchfork bifurcation known to lead to chimera states,^{10,12} whereas in large networks of ring and Erdős–Rényi topologies, the dynamics becomes immediately chaotic with several positive Lyapunov exponents. Numerical simulations reveal that this is a case of extensive chaos, a dynamical regime in which the dimension of the chaotic attractor increases

linearly with the system size. Extensive chaos, first conjectured by Ruelle,²¹ has been widely studied in spatially extended systems (usually under the more general term of “space–time chaos”),^{22–28} networks of spiking neurons,^{29,30} and mean-field models,³¹ among other systems. Nonetheless, to the best of our knowledge, this phenomenon had never been reported in networks of Kuramoto oscillators before.

Overall, our study presents a general analytical approach to study the dynamics of networks of identical Kuramoto–Sakaguchi populations and provides a direct link between the emergence of chimera states in two-population models and the appearance of extensive chaos in large networks of such populations.

II. A NETWORK OF KURAMOTO–SAKAGUCHI OSCILLATOR POPULATIONS

Let us consider N populations composed of M Kuramoto–Sakaguchi oscillators each.^{5,7} Each oscillator in a population is described by their phase variable $\phi_{j,\sigma}$ where $j \in \{1, \dots, M\}$ and $\sigma \in \{1, \dots, N\}$. The phase dynamics are given by

$$\dot{\phi}_{j,\sigma} = \omega_{j,\sigma} + \frac{K}{M} \sum_{\kappa=1}^N c_{\sigma\kappa} \sum_{m=1}^M \sin(\phi_{m,\kappa} - \phi_{j,\sigma} - \alpha), \quad (1)$$

where $\omega_{j,\sigma}$ are the natural frequencies of each oscillator, K is a global coupling strength parameter, and α is the Sakaguchi phase-shift parameter. In this equation, both the intra- and inter-population couplings are set via a mean-field, i.e., if populations σ and κ are coupled, then all oscillators in both populations contribute identically to the interaction. Therefore, the only source of irregularity in the interactions is set by the inter-population connectivity, which is determined by a weighted complex network with connectivity matrix $C = (c_{\sigma\kappa})$. We impose two constraints on this connectivity:

- We assume that C is row-normalized, i.e., $\sum_{\kappa=1}^N c_{\sigma\kappa} = 1$; thus, the total influence received by each oscillator is the same across populations.
- We assume that C is diagonalizable. This condition is always fulfilled if the network is undirected.

Generally, we focus on cases where the internal coupling within each population is larger than the coupling between other populations, i.e., $c_{\sigma\sigma} > c_{\sigma\kappa}$, for all $\sigma \neq \kappa$. Nonetheless, this is not a strict requirement.

The natural frequencies of the oscillators $\omega_{j,\sigma}$ are distributed according to a Cauchy (Lorenz) distribution centered at $\bar{\omega}$ and with half-width at half-maximum Δ . Due to the rotational symmetry of the model, we can set $\bar{\omega} = \tan(\alpha)(K \cos(\alpha) - \Delta)$ without loss of generality, a choice that will be justified in Sec. III.

The complex Kuramoto order parameter of each population reads

$$Z_\sigma = R_\sigma e^{i\Phi_\sigma} = \frac{1}{M} \sum_{m=1}^M e^{i\phi_{m,\sigma}}. \quad (2)$$

By considering now that $M \rightarrow \infty$, we can apply the Ott–Antonsen ansatz⁶ to obtain the evolution of Z_σ :

$$\dot{Z}_\sigma = (-\Delta + i\bar{\omega})Z_\sigma + \frac{K}{2} \sum_{\kappa=1}^N c_{\sigma\kappa} (Z_\kappa e^{-i\alpha} - Z_\sigma^2 Z_\kappa^* e^{i\alpha}). \quad (3)$$

This equation provides the mean-field dynamics of each population in the network assuming the phases follow a circular Cauchy distribution (Poisson kernel). Moreover, it has been recently shown that this ansatz is a global attractor of the Kuramoto–Sakaguchi model for $\Delta > 0$.³² Therefore, Eq. (3) is going to be our main object of study for the rest of the article.

III. ANALYSIS OF HOMOGENEOUS STATES AND THEIR STABILITY

In order to explore the dynamics of Eq. (3), first we study its homogeneous manifold, i.e., all the states in which the N populations evolve with exactly the same dynamics. By imposing $Z_\sigma = Z \forall \sigma$ into Eq. (3) and exploiting the fact that C is row-normalized, we obtain

$$\dot{Z} = (-\Delta + i\bar{\omega})Z + \frac{K}{2} (Z e^{-i\alpha} - Z^2 Z^* e^{i\alpha}), \quad (4)$$

which corresponds to the mean-field equation for a single, isolated population of Kuramoto–Sakaguchi oscillators.^{6,7} The dynamics of this system are well studied: If $K < K_c := \frac{2\Delta}{\cos(\alpha)}$, the system converges to the incoherent state $Z := 0$. At $K = K_c$, the system undergoes a supercritical Hopf bifurcation (H_0 in the figures) giving rise to a synchronized or coherent state, which takes the form $Z := R e^{i\Omega t}$, with

$$R = \sqrt{1 - \frac{2\Delta}{K \cos(\alpha)}} \quad (5)$$

$$\Omega = \bar{\omega} - \tan(\alpha)(K \cos(\alpha) - \Delta).$$

These equations show that our choice of the mean frequency $\bar{\omega} = \tan(\alpha)(K \cos(\alpha) - \Delta)$ defines a co-rotating frame in which the homogeneous coherent solution is a steady state rather than a limit-cycle (i.e., $\Omega = 0$). This simplifies the analytical calculations that follow.

Next, we focus on the stability of the coherent homogeneous state $Z > 0$ given by Eq. (5). The same analysis for the incoherent homogeneous solution $Z = 0$ is provided in Appendix D, where we show that no instabilities occur below the Kuramoto synchronization transition H_0 . Let us consider a small perturbation of the coherent homogeneous state, $Z_\sigma = Z + z_\sigma$. Linearizing Eq. (3), we obtain

$$\dot{z}_\sigma = (-\Delta + i\bar{\omega} - KR^2 e^{i\alpha}) z_\sigma + \frac{K}{2} \sum_{\kappa=1}^M c_{\sigma\kappa} (z_\kappa e^{-i\alpha} - R^2 z_\kappa^* e^{i\alpha}). \quad (6)$$

In order to simplify the notation, in the following steps, we express complex quantities in vectorial form: $z = (x, y)^T$, where x and y are the real and imaginary parts of z , respectively. Then, Eq. (6)

can be expressed as

$$\dot{z}_\sigma = Az_\sigma + B \sum_{\kappa=1}^M c_{\sigma\kappa} z_\kappa, \quad (7)$$

where

$$A = \begin{pmatrix} \Delta - K \cos(\alpha) & -\Delta \tan(\alpha) \\ \Delta \tan(\alpha) & \Delta - K \cos(\alpha) \end{pmatrix} \quad (8)$$

and

$$B = \begin{pmatrix} \Delta & \Delta \tan(\alpha) \\ -K \sin(\alpha) + \Delta \tan(\alpha) & K \cos(\alpha) - \Delta \end{pmatrix}. \quad (9)$$

These expressions for A and B are obtained by inserting the values of $\bar{\omega}$ and R derived from Eq. (5) into Eq. (6) and separating real and imaginary parts.

Next, we apply the master stability formalism (MSF),²⁰ in order to simplify the analysis of Eq. (7).³³ This method consists of decomposing the perturbation z_σ on the basis provided by the diagonalization of the connectivity matrix C . We denote the eigenvalues of the connectivity matrix as $\Lambda_1 \geq \Lambda_2 \geq \dots \geq \Lambda_N$ and the corresponding eigenvectors as $\Psi^{(k)} = (\Psi_1^{(k)}, \dots, \Psi_N^{(k)})^T$ with $k = 1, \dots, N$. Therefore,

$$C\Psi^{(k)} = \Lambda_k \Psi^{(k)}. \quad (10)$$

We now express the perturbation z_σ in the basis $\Psi^{(k)}$ as

$$z_\sigma = \sum_{k=1}^N u_k \otimes \Psi_\sigma^{(k)}, \quad (11)$$

where $u_k \in \mathbb{C}$ are the coordinates of z_σ in the new basis and \otimes is the Kronecker product.

Inserting Eq. (11) in the linearization provided by Eq. (6) and making use of Eq. (10), we derive the following expression:

$$\begin{aligned} \dot{z}_\sigma &= \sum_{k=1}^N \dot{u}_k \otimes \Psi_\sigma^{(k)} \\ &= A \sum_{k=1}^N u_k \otimes \Psi_\sigma^{(k)} + B \sum_{\kappa=1}^N c_{\sigma\kappa} \sum_{k=1}^N u_k \otimes \Psi_\kappa^{(k)} \\ &= \sum_{k=1}^N \left(A u_k \otimes \Psi_\sigma^{(k)} + B u_k \otimes \sum_{\kappa=1}^N c_{\sigma\kappa} \Psi_\kappa^{(k)} \right) \\ &= \sum_{k=1}^N (A u_k \otimes \Psi_\sigma^{(k)} + \Lambda_k B u_k \otimes \Psi_\sigma^{(k)}) \\ &= \sum_{k=1}^N (A + \Lambda_k B) u_k \otimes \Psi_\sigma^{(k)}. \end{aligned} \quad (12)$$

Since the eigenvectors $\Psi^{(k)}$ are a basis of \mathbb{R}^N , linear independence provides

$$\dot{u}_k = (A + \Lambda_k B) u_k. \quad (13)$$

Therefore, we decomposed the $2N \times 2N$ linear system Eq. (7) into N two-dimensional linear systems that depend on the eigenvalues Λ_k .

The eigenvalues $\lambda_k^{(\pm)}$ of the matrices $A + \Lambda_k B$ for $k = 1, \dots, N$ characterize the stability of the homogeneous solution (5). In fact, they correspond to the *Floquet exponents* of the periodic solution $Z = R e^{i\Omega t}$. The analytical expression for the eigenvalues reads,

$$\begin{aligned} \lambda_k^{(\pm)} &= \Delta + K \cos(\alpha) \left(\frac{\Lambda_k}{2} - 1 \right) \\ &\pm \left\{ \frac{K^2 \Lambda_k^2 \cos^2(\alpha)}{4} + K \Lambda_k \Delta \cos(\alpha) [\tan^2(\alpha)(1 - \Lambda_k) - \Lambda_k] \right. \\ &\quad \left. + \Delta^2 [(\Lambda_k^2 - 1) \tan^2(\alpha) + \Lambda_k^2] \right\}^{1/2}. \end{aligned} \quad (14)$$

This corresponds to a dispersion relation analogous to that in reaction-diffusion systems, with the structural eigenmodes $\Psi^{(k)}$ playing the role of wave functions.

The eigenvalues $\lambda_k^{(\pm)}$ depend explicitly on the parameters of the system (Δ , α , and K) as well as on the structural eigenvalues Λ_k . Using the row-normalization of C and the Gershgorin circle theorem,³⁴ we can assert that $|\Lambda_k| \leq 1$. Moreover, the largest structural eigenvalue is $\Lambda_1 = 1$, and the corresponding eigenvector corresponds to a uniform perturbation, i.e.,

$$\Psi^{(1)} = \frac{1}{\sqrt{N}} (1, \dots, 1)^T. \quad (15)$$

From the expression in Eq. (14), we see that $\lambda_1^{(+)} = 0$, as it should, since the homogeneous state is a limit-cycle in a co-rotating frame. The eigenvalues λ_k for $k > 1$ indicate the growth rates of perturbations that are transverse to the homogeneous manifold.

For the case $\Delta = 0$, the expression of the system eigenvalues simplifies to $\lambda_k^{(+)} = K \cos(\alpha)(\Lambda_k - 1)$ and $\lambda_k^{(-)} = -K \cos(\alpha)$. Since the coherent state emerges for $K \cos(\alpha) > 2\Delta = 0$, this proves that, in networks without disorder, the homogeneous state is always stable, consistent with the fact that chimera states in these systems always coexist with the fully synchronized solution.⁹

For $\Delta > 0$, however, the scenario changes. In this case, it is possible to perform a parameter reduction (see Appendix C). Setting $\Delta = 1$ without loss of generality, we analyze the system for different values of K and α . Figure 1(a) shows $\text{Re}[\lambda^{(\pm)}]$ as a function of Λ for different parameter sets. For the selected values, the dispersion relation displays a positive region, indicating the existence of transverse instabilities, which always emerge through real eigenvalues $\lambda^{(+)} \in \mathbb{R}$.³⁵ Overall, the shape of the dispersion relation resembles that of the Benjamin-Feir instability in the complex Ginzburg-Landau equation.³⁶

Setting $\text{Re}[\lambda^{(+)}] = 0$ in Eq. (14) determines the regions where transverse instabilities of the homogeneous state arise in parameter space. Figure 1(b) shows such regions for three different values of α in the (K, Λ) -plane. A small region of instabilities arise already for $\alpha = 1$ and widens as $\alpha \rightarrow \pi/2$, the critical value above which the homogeneous coherent solution vanishes completely. This is consistent with previous findings showing that chimera and other symmetry-breaking states emerge only for α close to, but below, $\pi/2$ ^{2,9,12,37} In particular, Wolfrum *et al.*³⁷ showed that, in a continuous media with nonlocal coupling, Benjamin-Feir instabilities of the homogeneous state arise only for values of α between $\pi/4$ and $\pi/2$.

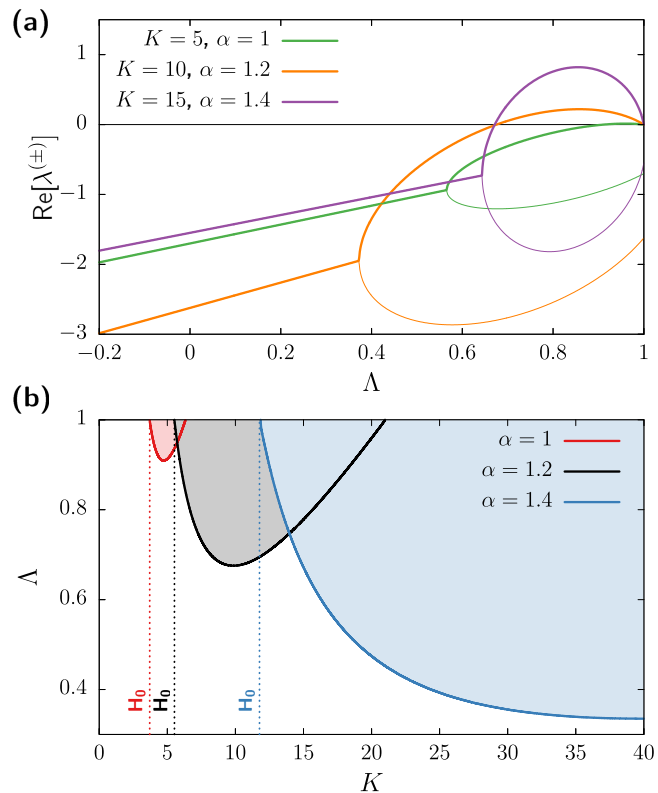


FIG. 1. Transverse instabilities of homogeneous states in networks of Kuramoto-Sakaguchi populations Eq. (3). (a) Real part of the eigenvalues (Floquet exponents) characterizing the stability of the homogeneous solution $\lambda^{(\pm)}$ as a function of the structural matrix eigenvalues Λ . Thick and thin curves correspond to $\lambda^{(+)}$ and $\lambda^{(-)}$ as given by the master stability function in Eq. (14), respectively. Green, orange, and purple curves correspond to $(K, \alpha) = (5, 1)$, $(10, 1.2)$, and $(15, 1.4)$. (b) Color-shaded regions show the regions of transverse instabilities in the (K, Λ) plane, with solid lines showing the loci of the bifurcation $[\text{Re}[\lambda^{(+)}] = 0$ in Eq. (14)]. Dotted vertical lines indicate the Kuramoto synchronization transition H_0 at which the coherent homogeneous solution emerges. Results shown for $\alpha = 1$ (red), 1.2 (black), and 1.4 (blue).

Our analysis provides an analogous picture only if Λ is regarded as continuous. For finite-size network topologies, transverse instabilities depend on the discrete network spectra, and specifically, the region of instability is determined by the second largest eigenvalue Λ_2 [see Fig. 1(b)]. Figure 2 shows how the region of transverse instabilities changes with Λ_2 in the (α, K) -plane. For $\Lambda_2 \rightarrow 1$, the bifurcation diagram approaches that of Kuramoto-Sakaguchi oscillators in a continuous array³⁸ [cf. Fig. 2(b) of Ref. 37]. For $\Lambda_2 < 1$, the instability region becomes smaller and with boundaries detached from the Kuramoto synchronization transition H_0 .

In Secs. IV–VI, we study how these bifurcation scenarios apply to a two-population model, ring networks, and Erdős-Rényi connectivities. For this analysis, we fix $\alpha = 1.2$, a value not that close to the limit case $\pi/2$ but still displaying a large instability region.

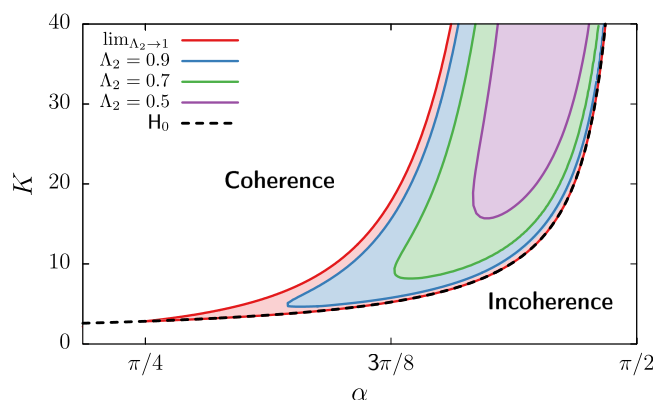


FIG. 2. Bifurcation diagram of networks of Kuramoto-Sakaguchi populations Eq. (3) with specific Δ_2 . Color-shaded areas indicate the regions of transverse instabilities for different values of the second largest structural eigenvalue Δ_2 . The dashed black curve indicates the Kuramoto synchronization transition H_0 .

IV. REVIEW OF THE TWO-POPULATION MODEL

As a first example, we revisit the two-population model. Previous works on this setup showed the emergence of chimera and other states from a pitchfork bifurcation of the homogeneous synchronized state if $\Delta > 0$.^{10–13} Here, we show that such bifurcation corresponds to a transverse instability provided by Eq. (14) and review some of the dynamics emerging from this symmetry-breaking. As in Sec. III, we fix $\Delta = 1$ without loss of generality (see Appendix C).

The connectivity matrix in the two-population model reads

$$C = \begin{pmatrix} \mu & 1-\mu \\ 1-\mu & \mu \end{pmatrix}. \quad (16)$$

where $\mu \in [0, 1]$ is a parameter controlling the coupling strength within the population, and $1 - \mu$ corresponds to the coupling strength across the two populations.

The eigenvalues of this connectivity matrix read $\Lambda_1 = 1$ and $\Lambda_2 = 2\mu - 1$. Substituting Λ_2 in Eq. (14) and setting $\text{Re}[\lambda_2^{(+)}] = 0$ provide an analytical expression for the pitchfork bifurcation of the homogeneous state as an implicit equation on the system parameters. The solid black curve in Fig. 3(a) shows such bifurcation line in the (K, μ) -plane, with the color-shaded regions above the line indicating the areas where the homogeneous state is unstable [see also black curve in Fig. 1(b)]. Within this region, four different states might exist (apart from the incoherent and coherent homogeneous states):⁴⁰

- **Steady chimera** [pink region in Fig. 3(a)], a fixed point characterized by $R_1 \neq R_2$.
- **Breathing chimera** [yellow region in Fig. 3(a)], a limit-cycle characterized by one population having always a larger degree of synchrony than the other, i.e., either $R_1(t) > R_2(t)$ or $R_2(t) > R_1(t)$ for all $t > 0$ [see Fig. 4(a)].
- **Symmetric limit-cycle** [green and blue regions in Fig. 3(a)], characterized by $R_1(t) = R_2(t + T/2)$, where T is the period of the oscillation [see Fig. 4(b)].

- **Antiphase fixed point** [blue and purple regions in Fig. 3(a)], characterized by $R_1(t) = R_2(t)$ but $\Phi_1 - \Phi_2 = \pi$. A thorough analysis of this state, including its linear stability, is provided in Appendix F.

In order to illustrate the emergence and nature of these different states, we first fix $\mu = 0.9$ and study the system dynamics upon increasing K with the help of numerical continuation software.³⁹ The resulting bifurcation diagram is depicted in Figs. 3(b) and 3(c) and can be split in nine different regions (labelled i-ix) delimited by different bifurcations:

- (i) For $K < K_c \approx 5.52$, the incoherent state $Z_\sigma = 0$ is the only stable solution. This state loses stability at the Kuramoto synchronization transition H_0 , leading to the emergence of the coherent homogeneous state.
- (ii) The coherent homogeneous state is the global attractor of the system from H_0 up to $K \approx 6.66$, when it loses stability through the supercritical pitchfork bifurcation (PF+) given by Eq. (14).
- (iii) Above PF+, two stable fixed points emerge, corresponding to steady chimeras [black lines in Fig. 3(b), pink-shaded region]. Although the steady chimeras coexist with the unstable homogeneous and antiphase fixed points, they are the sole attractor in this region of the parameter space.
- (iv) At $K \approx 7.37$, the steady chimeras undergo a supercritical Hopf bifurcation (H+) leading to the emergence of two stable limit-cycles, corresponding to the breathing chimera [red lines in Fig. 3(b), yellow-shaded region]. Figure 4(a) shows exemplary time series of this state, and Fig. 4(c) shows the corresponding phase portrait, with black curves depicting the limit-cycles and the red curve showing an example of a trajectory.
- (v) The breathing chimera limit-cycles eventually collide with the unstable coherent homogeneous state at $K \approx 7.89$, merging in a single limit-cycle through a double homoclinic bifurcation (Dhom., also known as *gluing bifurcation*)^{11,41,42}. The resulting attractor corresponds to a symmetric limit cycle in which the two populations alternate the same level of synchrony half a period apart [red lines in Fig. 3(b), green-shaded region]. Figure 4(b) shows exemplary time series of this regime, and Figs. 4(d) and 4(e) depict two phase portraits, with K in panel (d) very close to the gluing bifurcation.
- (vi) At $K \approx 9.19$, the antiphase state of the system, which is unstable for smaller values of K , becomes stable through a subcritical Hopf bifurcation (H-, see Appendix F). Therefore, in this region of the bifurcation diagram, there is bistability between the antiphase state and the symmetric limit-cycle [black and red lines in Fig. 3(b), blue-shaded region]. Figure 4(f) shows the phase portrait of this bistable regime, with the unstable limit-cycle represented by a gray curve.
- (vii) The symmetric limit-cycle collides with the unstable limit-cycle at $K \approx 9.41$, thus both solutions vanish through a saddle-node of limit-cycles (SNLC). Then, the antiphase state becomes the only attractor for a wide region of the parameter space [black curve in Figs. 3(b) and 3(c), purple-shaded region].
- (viii) At $K \approx 15.67$, the homogeneous fixed point recovers stability through the (subcritical) pitchfork bifurcation provided by Eq. (14) [see PF- in Fig. 3(c)]. Therefore, in this region,

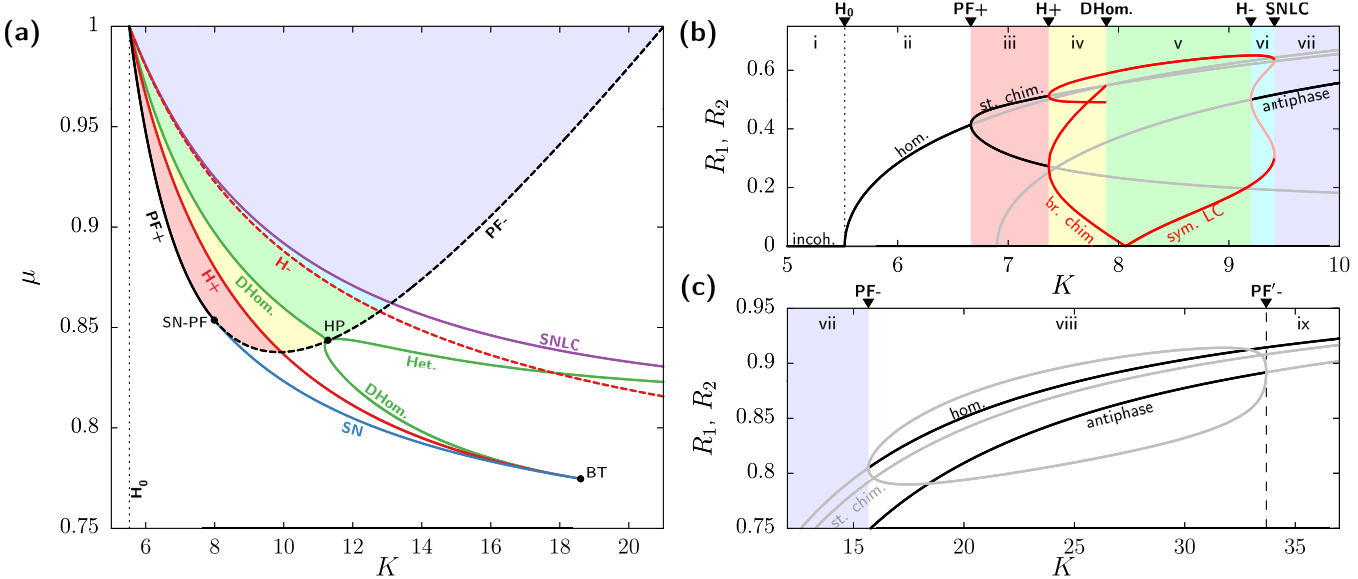


FIG. 3. Bifurcation diagrams of the two population model [Eq. (3) with Eq. (16)] for $\alpha = 1.2$ and $\Delta = 1$. (a) Two-parameter bifurcation diagram. Solid lines indicate supercritical bifurcations (+) and dashed lines indicate subcritical bifurcations (-). Black curves correspond to the pitchfork bifurcation (PF) of the homogeneous state [given by Eq. (14)], red curves indicate Hopf bifurcations (H), green curves indicate double homoclinic (DHom.) and heteroclinic (Het.) bifurcations, the blue curve indicates a saddle-node bifurcation (SN), and the purple curve indicates a saddle-node of limit-cycles (SNLC). Straight dotted thin line indicates the Kuramoto synchronization transition (H_0). Color-shaded regions indicate instability of the homogeneous solution, with each color corresponding to a different attractor set: Pink for stable steady chimeras, yellow for breathing chimeras, green for symmetric oscillations, blue for bistability between symmetric oscillations and antiphase state, and purple for stability of the antiphase fixed point only. (b) and (c) One-parameter bifurcation diagram for $\mu = 0.9$. Solid curves with different colors indicate different attractor types: Black for stable fixed points, gray for unstable fixed points, red for stable limit-cycles, and light red for unstable limit-cycles. Relevant bifurcations are labelled on the top of the figures, with the different regions between bifurcations shaded with the same color scheme as in panel (a). Homogeneous and antiphase solutions together with their corresponding bifurcations ($H_0, PF, H-, PF'$) have been obtained analytically. All other results have been obtained with auto-07p³⁹ (see Appendix B).

both homogeneous and antiphase states share stability [black curves in Fig. 3(c)].

- (ix) Finally, the unstable fixed points emerging from PF_- collide with the antiphase solution at a new subcritical pitchfork bifurcation (PF'_-) at $K \approx 33.69$ (see Appendix F for an analytical derivation of PF'_-). From this point on, further increase in K does not lead to any other bifurcation, and the homogeneous state remains the only (global) attractor of the system [black curve in Fig. 3(c)].

The two-parameter bifurcation diagram in Fig. 3(a) shows that the bifurcation scenario we have described for $\mu = 0.9$ holds for the entire region of instability of the homogeneous state. The diagram also shows the loci of a saddle node bifurcation (SN) that joins the pitchfork bifurcation (PF) at a fold-pitchfork codimension-2 bifurcation (SN-PF). At this codimension 2 point, the symmetry breaking bifurcation turns from supercritical to subcritical.^{10,12} This SN branch limits a region of bistability between the homogeneous fixed point and stable chimeras. Within this region, following a route similar to the one described before, the stable chimera turns into a breathing state at the supercritical Hopf (H+). Nonetheless, in this case, the gluing bifurcation leads to the disappearance of limit-cycle solutions since the homogeneous state is stable. Finally, there is an additional region of bistability between the symmetric limit cycle

and the homogeneous state bounded by a heteroclinic bifurcation and the saddle-node of limit cycles (SNLC).

Altogether, this analysis reveals a rich dynamical landscape emerging from the pitchfork bifurcation that breaks the symmetry of the homogeneous state. These results complement those presented in previous works for the same system^{10–13} but without relying on weak heterogeneity. Moreover, the pitchfork bifurcation of the homogeneous state (PF) and the bifurcations from the antiphase state (H- and PF'_-) have been obtained analytically as implicit equations on the system parameters.

V. RING TOPOLOGY

Now, we consider a ring network composed of $N > 2$ populations connected via nearest neighbors. The connectivity matrix $C = (c_{\sigma\kappa})$ reads

$$c_{\sigma\kappa} = \begin{cases} \mu & \text{if } \sigma = \kappa \\ \frac{1-\mu}{2} & \text{if } |\sigma - \kappa| = 1 \text{ or } N-1 \\ 0 & \text{otherwise.} \end{cases} \quad (17)$$

This scenario was studied by Lee *et al.*¹⁸ for the case of $N = 6$ oscillators, where they unveiled different forms of stable and (non-chaotic) breathing chimera states for heterogeneous populations.

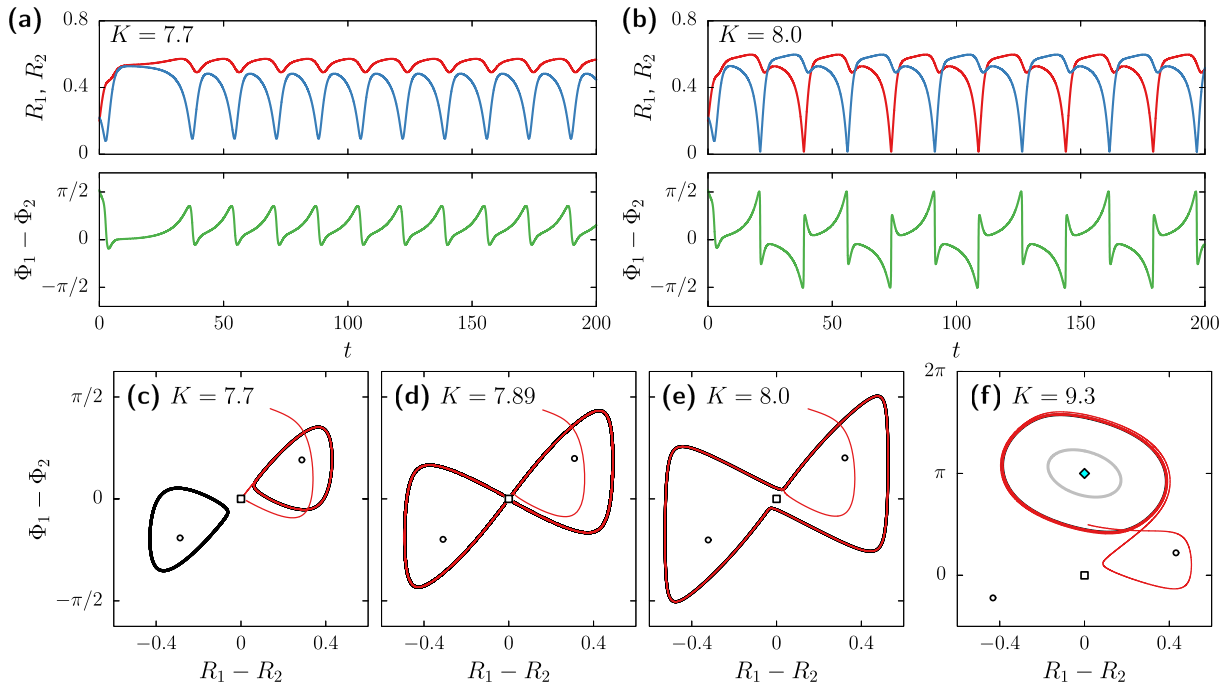


FIG. 4. Oscillatory dynamics in the two-population Kuramoto model [Eq. (3) with Eq. (16)] for $\mu = 0.9$, $\alpha = 1.2$, and $\Delta = 1$. (a) and (b) Time series of the Kuramoto order parameters and phase difference of the two populations at a breathing chimera state [panel (a), $K = 7.7$] and symmetric limit-cycle [panel (b), $K = 8$]. (c)–(f) Phase portraits for different values of K showing breathing chimera [panel (c)], the symmetric limit-cycle [panels (d) and (e)], and bistability between the antiphase state and the symmetric limit-cycle [panel (f)]. Bold black curves show the stable limit-cycles and red curves show an exemplary trajectory. Gray curve in panel (f) shows the unstable limit-cycle. Open symbols correspond to the different unstable fixed points: square (\square) indicates the homogeneous state and circles (\circ) indicate the two steady chimera states. Blue-colored diamond (\diamond) in panel (f) indicates the stable antiphase state.

Also, Laing¹⁹ analyzed a similar ring model but with non-local coupling, which displayed chaotic solutions that vanish upon increasing system size. Here, we show that, in our setup, transverse instabilities of the homogeneous state lead to chaotic dynamics that show an extensive character with N , i.e., the dynamical complexity of the system scales linearly with the system size.

Since C is a circulant matrix, its eigenvalues have a simple expression. In order to preserve the ordering from larger to smaller, we write them as

$$\Lambda_k = \begin{cases} \mu + (1 - \mu) \cos\left(\frac{\pi}{N}(k - 1)\right) & \text{if } k \text{ is odd,} \\ \mu + (1 - \mu) \cos\left(\frac{\pi}{N}k\right) & \text{if } k \text{ is even,} \end{cases} \quad (18)$$

for $k = 1, \dots, N$. The corresponding eigenvectors are the discrete Fourier modes

$$\Psi_j^{(k)} = \begin{cases} \frac{\pi j}{N} e^{\frac{\pi j}{N}(k-1)i} & \text{if } k \text{ is odd,} \\ \frac{\sqrt{N}}{\pi j} e^{-\frac{\pi j}{N}ki} & \text{if } k \text{ is even,} \end{cases} \quad (19)$$

where $k = 1, \dots, N$.

As N increases, the second largest structural eigenvalue Λ_2 tends to 1. Therefore, from Figs. 1(b) and 2, we infer that the region of transverse instability expands with N . Figure 5(a) illustrates this situation: Thick continuous curves depict the bifurcation obtained in the (K, μ) -plane by setting $\text{Re}[\lambda^{(+)}] = 0$ in Eq. (14). As N increases, the region of instability becomes larger, covering a wideband of K values irrespective of μ if N is sufficiently large. Moreover, the emergence of instabilities occurs arbitrarily close to the Kuramoto synchronization transition [H_0 , vertical black dashed line in Fig. 5(a)].

Another important aspect of the ring spectrum in Eq. (18) is that it is delocalized, i.e., it covers the interval $\Lambda_k \in [2\mu - 1, 1]$ densely as $N \rightarrow \infty$. Therefore, several structural eigenmodes Λ_k might concurrently correspond to different unstable directions. For instance, the colored region in Fig. 5(b) shows the number of unstable directions of the homogeneous state in the (K, μ) -plane for $N = 128$. The number of positive growth rates generally increases with μ , with a large region (dark blue) where all $\lambda_k^{(+)} > 0$ for $k > 1$. In fact, this region coincides with the region of transverse instability for the two-population model, since the last mode turning unstable corresponds to $\Lambda_N = 2\mu - 1$.

The regularity of ring topologies also allows for the existence of twisted states,^{18,43} i.e., traveling wave solutions of the form $Z_\sigma = \tilde{R} e^{\tilde{\Omega}t + \frac{2\pi}{N}q\sigma}$ where $q \in \mathbb{Z}$ is the winding number. These states

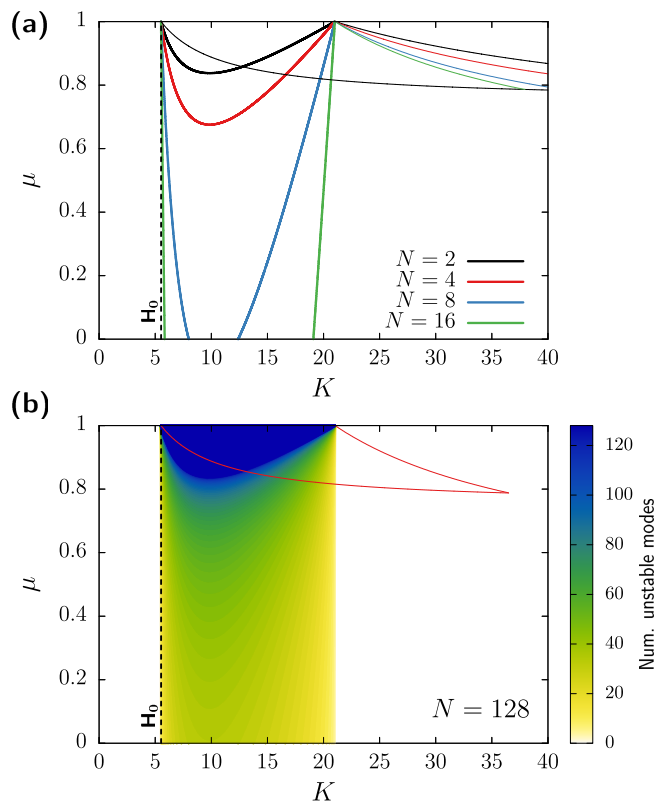


FIG. 5. Transverse instabilities of the homogeneous and antiphase state in ring networks ($\alpha = 1.2$ and $\Delta = 1$). (a) Regions contained within the thick lines correspond to transverse instabilities of the homogeneous state for different N . Regions contained within the thin curves indicate stability of the antiphase state. (b) Color-shaded regions show the number of unstable modes of the homogeneous state for a network of $N = 128$ populations. Red curve encloses the region of stability of the antiphase state. Vertical black dashed line indicates the Kuramoto synchronization (H_0) transition in both panels.

have been studied in the context of the Kuramoto model in spatially extended arrays with nonlocal coupling^{37,43} and also networks of populations,¹⁸ where they have shown to play a major role on the emergence of nontrivial dynamics. For our particular choice of nearest neighbor coupling, twisted states emerge but do not seem to play a prominent role on the emergence of complex dynamics. In Appendix E, we provide a detailed discussion of these states, including linear stability and bifurcation diagrams. Altogether, we find that, for our choice of C , most twisted states are stable only for large K , for which the homogeneous state is already stable (see Fig. 10). The only exception to this picture are twisted states with winding number $q = N/2$ (i.e., antiphase states) and $q = N/3$, provided they exist. Thin lines in Fig. 5(a) and the red line in Fig. 5(b) delimit the region of stable antiphase dynamics in ring networks of different sizes. Although this region shrinks by increasing N , it does not vanish and intersects a significant portion of the region of transverse instabilities of the homogeneous state (see Appendix F for a simplified linear stability analysis for antiphase states in ring networks).

Overall, in large ring networks, we expect to have complex dynamics in wide regions of parameter space due to the expansion of the transverse instability region and the number of unstable directions of the homogeneous state. Figure 6 shows two instances of these complex dynamics for $N = 128$. Panel (a) depicts R_σ and Φ_σ of each population over time for parameters in the region where the number of unstable directions of the homogeneous state is maximal ($K = 7$, $\mu = 0.9$). The dynamics of R_σ are rather disordered, with ϕ_σ showing some indications of spatial structure. Instead, panel (b) corresponds to parameters associated with less unstable directions ($K = 15$, $\mu = 0.5$). In this case, the dynamics of both R_σ and Φ_σ evolve more regularly, in spite of their seemingly chaotic behavior. These qualitative observations posit the existence of space-time chaos emerging from the transverse instabilities reported here. In the rest of this section, we assess the chaotic and complex behavior of the system by means of numerical Lyapunov analysis. Appendix A contains precise definitions of the monitored quantities.

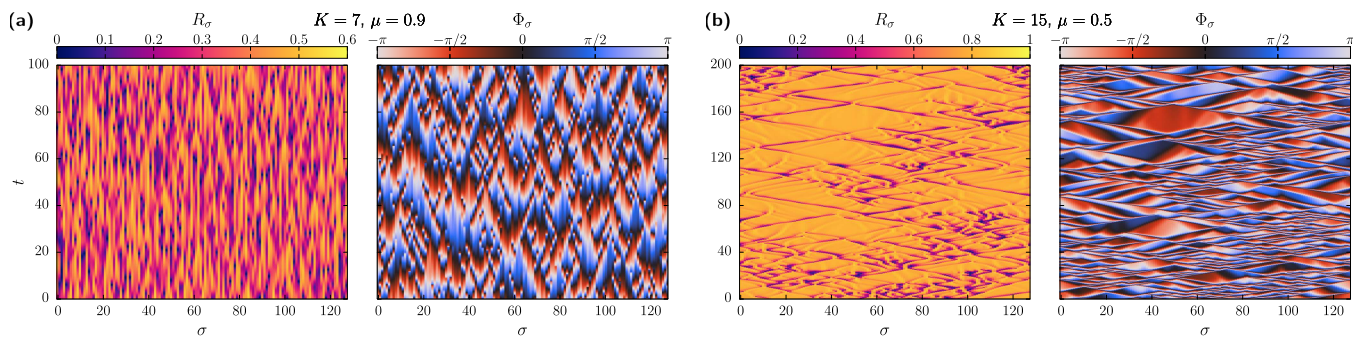


FIG. 6. Chaotic dynamics of the ring model for different parameter values ($\alpha = 1.2$ and $\Delta = 1$). (a) Kuramoto order parameter of each population R_σ and corresponding phase Φ_σ for $K = 7$ and $\mu = 0.9$ after a transient of 1000 time units. (b) Same quantities for $K = 15$ and $\mu = 0.5$.

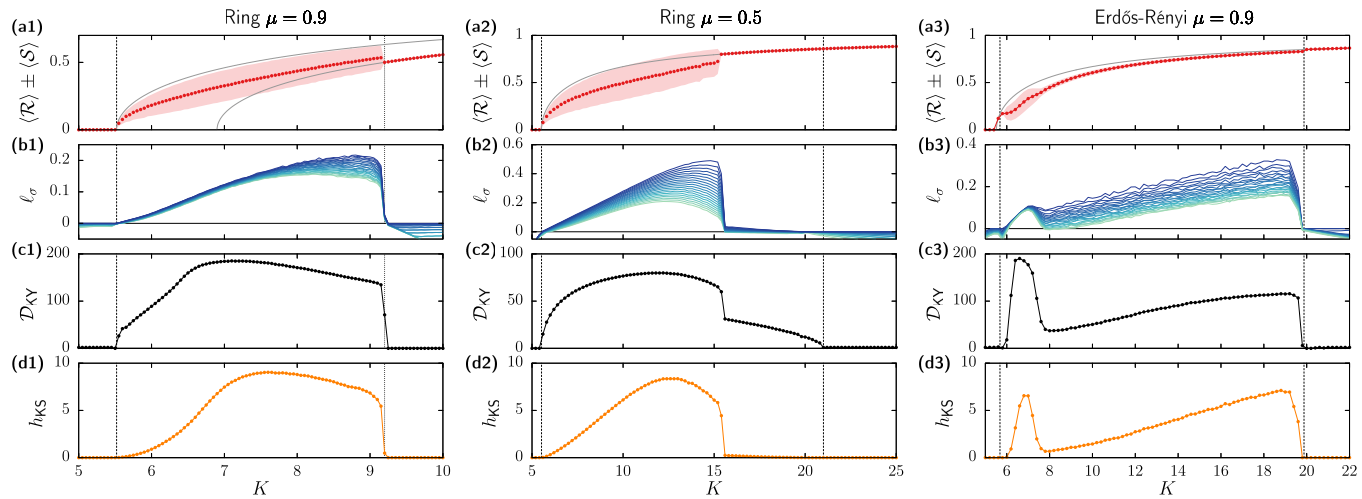


FIG. 7. Simulations of ring (columns 1 and 2) and Erdős–Rényi (column 3) networks with $N = 128$ ($\alpha = 1.2$ and $\Delta = 1$). (a) Red circles indicate time average mean activity $\langle \mathcal{R} \rangle$, with the red-shaded region showing the corresponding level of heterogeneity $\langle \mathcal{R} \rangle \pm \langle S \rangle$. Gray curves correspond to the value of R for the homogeneous states given by Eq. (5). In panel (a1), an additional gray curve shows the antiphase state [Eq. (F2)]. (b) 20 largest Lyapunov exponents ℓ_σ . (c) Kaplan–Yorke fractal dimension computed using the (complete) Lyapunov spectra as given by Eq. (A3). (d) Kolmogorov–Sinai dynamical entropy computed from Eq. (A4). In all panels, vertical dashed lines indicate the emergence and disappearance of transverse instabilities as given by Eq. (14). Dotted vertical line in panels (a1)–(d1) indicates the emergence of stable antiphase state as given by Eq. (F8).

First, we focus on a fixed network size ($N = 128$) and study the dynamics by varying K . Figures 7(a1)–7(d1) show the numerical results obtained with fixed $\mu = 0.9$, thus covering the region of maximal number of instabilities. The red circles in Fig. 7(a1) show the time average of the network’s mean Kuramoto order parameter, \mathcal{R} . The shaded region shows the corresponding standard deviation S (see Appendix A for specific definitions). The gray continuous lines indicate the value of \mathcal{R} corresponding to the homogeneous and antiphase states [Eqs. (5) and (F2)]. As predicted, the nontrivial dynamics emerge just after the Kuramoto transition to synchrony H_0 and appear to be the only attracting state until the stabilization of the antiphase state (see dotted vertical lines).

To characterize the complexity of these non-trivial states, Fig. 7(b1) displays the 20 largest Lyapunov exponents ℓ_σ of the network. At the transverse instability, many exponents become positive at once, thus indicating the emergence of high-dimensional chaotic dynamics. Indeed, the Kaplan–Yorke formula [Fig. 7(c1)] indicates a fractal dimension with about $\mathcal{D}_{KY} \approx 28$ degrees of freedom just after the transition. The attractor dimension increases smoothly until it reaches a maximum of $\mathcal{D}_{KY} \approx 200$ and then slowly decreases until vanishing at the stabilization of the antiphase state. Similarly, the Kolmogorov–Sinai dynamical entropy h_{KS} [Fig. 7(d1)] also increases starting at the transverse instability, albeit it does so less abruptly. This measure indicates that the maximum complexity of the trajectories is reached around $K \approx 7.5$. Altogether, these results establish the existence of high-dimensional chaos arising from the transverse instabilities of the homogeneous state for $\mu = 0.9$.

Next, we switch to $\mu = 0.5$, for which the homogeneous state has fewer unstable directions. Moreover, the antiphase state does not exist for this value of μ , and therefore, we expect non-trivial dynamics for a larger K -range (note the difference in the x-axis range

between columns 1 and 2 in Fig. 7). Figures 7(a2)–7(d2) show that the scenario starts off analogously to that of $\mu = 0.9$: At the transverse instability (see vertical dotted line), the system transitions from incoherence to a state with a large degree of heterogeneity. Also, several Lyapunov exponents become positive at once, resulting into both \mathcal{D}_{KY} and h_{KS} increasing rapidly. Again, this corresponds to a case of space–time chaos.

Around $K \approx 15.8$ a transition occurs and the irregularity of the system drops drastically. The dynamics emerging from this bifurcation, which is not detected by our theory, proved challenging to characterize. First, the system suddenly evolves very close to the homogeneous state. In fact, our measure of network heterogeneity S is too small to be visually appreciated above the transition in Fig. 7(a2) (see pink shaded region). Nonetheless, a close inspection of the simulations (not shown) revealed irregular patterns in both R_σ and Φ_σ . Second, such spatiotemporal dynamics evolve slowly compared to the states encountered so far, requiring longer simulations (see Appendix B). Such slow time scales are mainly reflected by the magnitude of the positive Lyapunov exponents in Fig. 7(b2) and the drop on dynamical entropy shown in Fig. 7(d2). In spite of these peculiarities, the number of positive Lyapunov exponents and thus the value of \mathcal{D}_{KY} for $15.8 \lesssim K \lesssim 21$ [see Fig. 7(c3)] indicate that this corresponds to a high-dimensional chaotic regime.⁴⁴ Finally, around $K \approx 21.6$, the dynamics fall back to the homogeneous state, as predicted by the stability analysis (second vertical dashed line in the middle-row panels of Fig. 7).

So far, the numerical exploration for $\mu = 0.9$ and $\mu = 0.5$ proved the existence of highly complex spatiotemporal regimes emerging from transverse instabilities of the homogeneous state in rings of $N = 128$ populations. Next, we test the robustness and scaling these results upon varying the system size N . Figure 8 shows

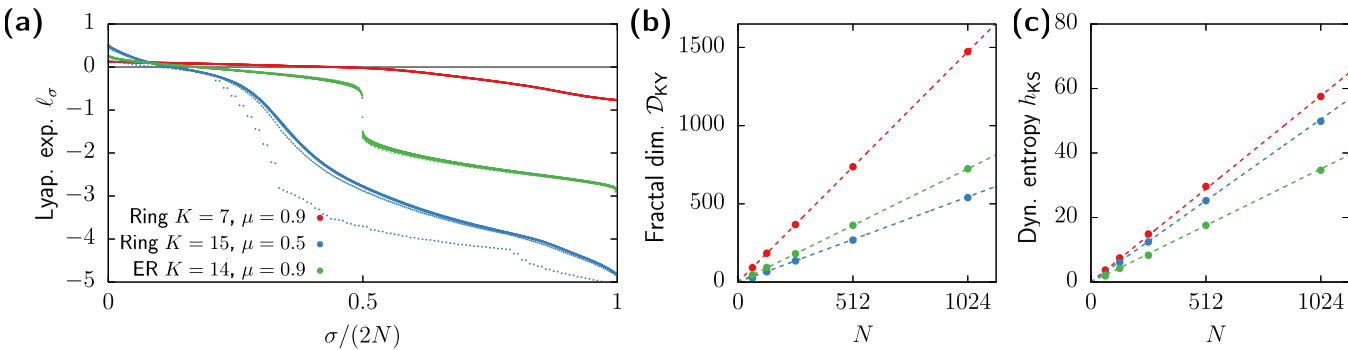


FIG. 8. Extensivity of chaos in ring and Erdős–Rényi (ER) networks ($\alpha = 1.2$ and $\Delta = 1$). (a) Complete Lyapunov spectra for different network sizes for the simulations of the ring and ER networks. For each parameter set, dots indicate the results for networks with $N = 64, 128, 256, 512$, and 1024 populations. Nonetheless, in most cases, differences across system sizes are barely visible. (b) and (c) Fractal dimension D_{KY} (panel b) and dynamical entropy h_{KS} (panel c) computed for different system sizes N in three different simulation setups. Circles correspond to numerical simulations. Dashed lines correspond to a linear regression. In all these plots, red corresponds to ring networks with $K = 7$ and $\mu = 0.9$, blue corresponds to ring networks with $K = 15$ and $\mu = 0.5$, and green corresponds to ER networks with $K = 14$ and $\mu = 0.9$.

results from simulations of rings composed of an increasing number N of oscillators (red and blue symbols) for selected parameter values. Panel (a) shows the Lyapunov spectra computed for different system sizes with node index normalized by the system size $\sigma/(2N)$. For the tested parameter values ((K, μ) = (7, 0.9), red symbols, and (15, 0.5), blue symbols), the spectra show a good collapse upon increasing N , i.e., the Lyapunov exponents converge to a well-defined profile, with the only exception of the smaller networks for the second set (blue dots). These robust spectra for increasing N indicate extensive chaos, i.e., a chaotic regime whose complexity scales linearly with the system size. To further explore this possibility, Figs. 8(b) and 8(c) show the computed fractal dimension and dynamical entropy for the same parameter values upon increasing N . In all cases, an accurate scaling $D_{\text{KY}} \propto N$ and $h_{\text{KS}} \propto N$ is observed.

Overall, these numerical results indicate that transverse instabilities of a homogeneous state lead to extensive chaos in ring networks of oscillator populations with nearest neighbor coupling. In the next section, we investigate the case of irregular topologies.

VI. ERDŐS–RÉNYI NETWORKS

Here, we discuss the dynamics that emerge in irregular network topologies. In order to simplify the analysis, we restrict ourselves on connectivities derived from Erdős–Rényi (ER) networks with fixed average degree $\bar{d} = 10$. Let $A = (a_{\sigma\kappa})$ be the adjacency matrix of an (undirected) Erdős–Rényi network (i.e., $a_{\sigma\kappa} \in \{1, 0\}$). Then, we consider a connectivity matrix $C = (c_{\sigma\kappa})$ given by

$$c_{\sigma\kappa} = \begin{cases} \mu & \text{if } \sigma = \kappa \\ \frac{1-\mu}{d_\sigma} a_{\sigma\kappa} & \text{if } \sigma \neq \kappa, \end{cases} \quad (20)$$

where d_σ is the degree of node σ in the Erdős–Rényi model. This connectivity preserves row-normalization, as required for the existence of homogeneous states, as well as introduces the self-coupling strength parameter μ .

Unlike the ring scenario, we are unaware of explicit analytical results on the spectra of C (which does not need to coincide with the spectra of the adjacency matrix A). However, combining analytical arguments with a numerical exploration, we can provide an accurate estimation of the region of transverse instabilities. By the Gershgorin circle theorem,³⁴ the eigenvalues of C are contained in the interval $\Lambda_k \in [1, 2\mu - 1]$. Therefore, based on Fig. 1(b), transverse instabilities of the homogeneous state will occur. The shape of the region will depend on the second largest eigenvalue Λ_2 . If $\tilde{\Lambda}$ is an eigenvalue of the matrix $D^{-1}A = (a_{\sigma\kappa}/d_\sigma)$, then $\Lambda = \mu + (1 - \mu)\tilde{\Lambda}$ is an eigenvalue of C . Averages over 100 simulated networks with different sizes (not shown) indicate that $\tilde{\Lambda}$ are densely distributed in the interval [-0.6, 0.6]. In particular, $\tilde{\Lambda}_2 \approx 0.6$ as N increases, and therefore, $\Lambda_2 \approx 0.4\mu + 0.6$. Using this approximation in the MSF,

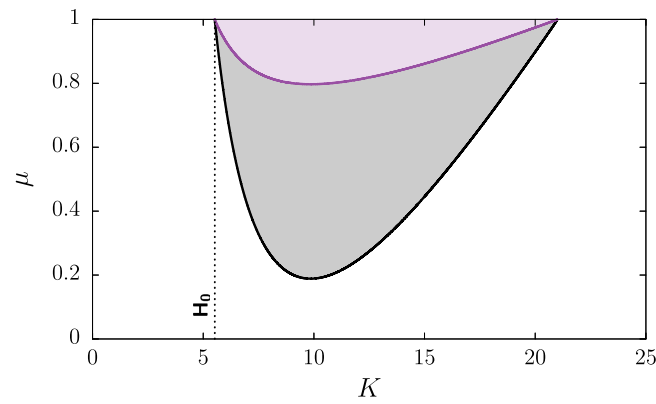


FIG. 9. Approximated region of transverse instabilities of the homogeneous state in Erdős–Rényi networks with average degree $\bar{d} = 10$. The gray-shaded region indicates where at least one mode is unstable (i.e., $\text{Re}[\lambda_2^{(+)}] > 0$). The purple-shaded region indicates where $N - 1$ modes are unstable. The vertical dashed line indicates the Kuramoto synchronization transition H_0 .

Eq. (14), provides the region of transverse instabilities for ER networks in the (K, μ) parameter space. The gray-shadowed region in Fig. 9 shows the area where at least one mode of the homogeneous state is unstable. Also in this case, the number of unstable directions in the region increases with N , with the purple region in Fig. 9 indicating the parameter values for which the homogeneous state has a maximum number of unstable modes ($N - 1$).

In order to capture the emergent dynamics, Figs. 7(a3)–7(d3) display the results of simulations performed with fixed $\mu = 0.9$ and different values of K for an ER network of $N = 128$ populations. As in the ring networks, the numerical outcome shows a scenario of consistent high-dimensional chaos for most of the transverse instability region (indicated by vertical dashed lines). Interestingly, two different types of complex dynamics seem to emerge: First, the level of heterogeneity captured by S shows a region of high dynamical variety among nodes [see red-shaded region in Fig. 7(a3), $6 \lesssim K \lesssim 8$]. In this case, the Lyapunov spectra show many exponents with similar positive values (panel b3), which translate into a very high Kaplan–Yorke dimension (panel c3) and dynamical entropy (panel d4). At $K \approx 8$, all measures show a significant reduction of complexity, indicating a transition to a different chaotic regime from $8 \lesssim K \lesssim 20$. In this case, the patterns lose heterogeneity, but the Lyapunov spectra still show a regime of high-dimensional chaos. In fact, the number and value of the largest exponents increase monotonically with K , leading to an equally gradual increase of D_{KY} and h_{KS} until the homogeneous state becomes stable again (at $K \approx 20$).

As in the ring model, we now test the robustness of the chaotic dynamics upon increasing network size. The green dots in Fig. 8(a) show the entire Lyapunov spectra for $K = 15$ and $\mu = 0.9$ upon increasing system size. Overall, the different spectra collapse to a single well-defined curve. Moreover, the green symbols in Figs. 8(b) and 8(c) indicate that both the fractal dimension and the dynamical entropy increase linearly with N , confirming thus the extensive nature of the chaotic regime in ER topologies.

VII. CONCLUSIONS

Recent works have studied the dynamics of networks of identical Kuramoto–Sakaguchi populations by means of the Ott–Antonsen equations under different parameter setups, coupling schemes, and system sizes.^{7,9–11,15–18,45} This paper provides a leap forward in these efforts by providing a general expression for the instabilities of the homogeneous state as a function of the eigenmodes of the structural connectivity matrix. We proved that, in networks without disorder ($\Delta = 0$), the homogeneous state is always transversally stable regardless of the topology. On the other hand, for disordered populations ($\Delta > 0$), transverse instabilities occur. These instabilities, which lead to chimera states in two-population networks,^{10,12,13} give rise to extensive chaos in large nearest-neighbor ring and random connectivity schemes.

The emergence of extensive chaos in ring networks could apparently conflict with the findings of Laing,¹⁹ which studied a similar setup but with non-local connectivity via a discrete kernel. In their work, the row-normalization of the connectivity matrix is preserved; thus, our theoretical framework also applies. The eigenvalues of their connectivity matrix can be analytically computed, and we found they are all zero except for three: $\Lambda_1 = 1$, $\Lambda_2 = \Lambda_3 >$

0. In particular, $\lim_{N \rightarrow \infty} \Lambda_2 = B/2$ where $B = 0.35$. This localized spectrum differs largely from the spectra of nearest neighbor ring topologies given by Eq. (18), which covers the interval $[2\mu - 1, 1]$ densely for large N . Although a more in-detail comparison between both setups is out of the scope of this paper, it is likely that the transverse instabilities reported in Ref. 19 only occur through Λ_2 and Λ_3 , rather than through several concurrently unstable eigenmodes. This might explain the disappearance of chaos for large networks in that setup.

These differences between non-local and local interactions in rings indicate that network topology and, specifically, their spectra, play an important role on the properties of the resulting dynamical states. Here, we restricted ourselves on simple structures, without an in-depth analysis of how specific topological features affect the emergent behavior. Future work should analyze the effect of varying network density in both ring and Erdős–Rényi networks and the impact of other topologies such as scale-free or small world.

On a different note, the extensive nature of the chaotic states and the patterns displayed in ring networks are an indication that this form of space–time chaos could correspond to a turbulent state. Interestingly, the dependence of the growth rates on the structural eigenmodes depicted in Fig. 1(a) resembles that of the Benjamin–Feir instability in the complex Ginzburg–Landau equation.⁴⁶ Similar turbulent states have been studied in arrays of individual Kuramoto–Sakaguchi oscillators with non-local coupling.^{37,47,48} Further analysis should, thus, address to what extent the properties of our setup for increasing N match those of phase or amplitude turbulence in spatially extended systems.³⁶

Here, we have studied the dynamics of the Kuramoto–Sakaguchi populations at the thermodynamic limit via the Ott–Antonsen equations. The global attractiveness of this low-dimensional manifold for $\Delta > 0$ has been recently proven,³² strengthening the validity of this approach to study networks of Kuramoto–Sakaguchi populations. Nonetheless, previous works have shown that (low-dimensional) chaotic dynamics in the Ott–Antonsen equations might display different properties in finite-size simulations.¹¹ A detailed comparison of simulations of the microscopic system (1) with finite M , and those of the Ott–Antonsen description Eq. (3), could provide valuable insights into understanding the convergence of Kuramoto–Sakaguchi ensembles to the low-dimensional manifold. Nonetheless, such study would require a considerable computational effort due to the large number of degrees of freedom involved.

Finally, although our study does not stem from any particular physical setup, the Kuramoto–Sakaguchi model successfully describes a wide variety of real-world phenomena, including power grids,⁴⁹ circadian rhythms,⁵⁰ and bacterial biofilms.⁵¹ A particularly explored application is neural dynamics, where the Kuramoto–Sakaguchi model has been rigorously derived from spiking neuron models.⁵² In this context, the mean-field description provided by the Ott–Antonsen equations leads to a simplified neural mass model.⁷ Thus, our analysis of the coupled system Eq. (3) provides a simple, yet grounded, framework to analyze whole brain dynamics where each brain region is represented by a Kuramoto–Sakaguchi population. In fact, the study of transverse instabilities in whole brain models is a powerful tool to unveil the

multiscale dynamics of these systems, even when the single-node dynamics evolve according to generic neural mass models.⁵³

ACKNOWLEDGMENTS

The authors would like to thank Diego Pazó and Alessandro Torcini for useful feedback on this work. P.C. and J.G.O. have received funding from the Future and Emerging Technologies Programme (FET) of the European Union's Horizon 2020 research and innovation programme (project NEUROTWIN, Grant Agreement No. 101017716). J.G.O. was also financially supported by the Spanish Ministry of Science and Innovation, the Spanish State Research Agency and FEDER (Project Reference No. PID2021-127311NB-I00), and by the ICREA Academia program. This work was done while P.F. was a student at the ETSETB, Universitat Politècnica de Catalunya.

AUTHOR DECLARATIONS

Conflict of Interest

The authors have no conflicts to disclose.

Author Contributions

Pol Floriach: Formal analysis (equal); Investigation (equal); Methodology (equal); Software (equal); Validation (equal); Visualization (equal); Writing – review & editing (equal). **Jordi Garcia-Ojalvo:** Funding acquisition (equal); Investigation (equal); Methodology (equal); Resources (equal); Supervision (equal); Validation (equal); Writing – review & editing (equal). **Pau Clusella:** Conceptualization (equal); Formal analysis (equal); Investigation (equal); Methodology (equal); Software (equal); Supervision (equal); Validation (equal); Visualization (equal); Writing – original draft (equal); Writing – review & editing (equal).

DATA AVAILABILITY

The data that support the findings of this study are openly available in Github at github.com/pclus/KuramotoPopulationNetwork, Ref. 60.

APPENDIX A: MEASURES OF COLLECTIVE ACTIVITY

Here, we describe the different quantitative measures employed to characterize the dynamics emerging from transverse instabilities in large networks of oscillator populations.

- To capture the macroscopic behavior of the system, we compute the mean Kuramoto order parameter,

$$\mathcal{R}(t) := \frac{1}{N} \sum_{\sigma=1}^N R_\sigma(t), \quad (\text{A1})$$

and its instantaneous standard deviation on the network

$$\mathcal{S}(t) = \frac{1}{\sqrt{N}} \left\{ \sum_{\sigma=1}^N [R_\sigma(t) - \mathcal{R}(t)]^2 \right\}^{\frac{1}{2}}. \quad (\text{A2})$$

If the network is at a heterogeneous state (in R_σ), then $\mathcal{S} > 0$.

- The chaotic activity of a system can be characterized by the corresponding Lyapunov exponents^{54,55} which we denote by ℓ_σ , where $\ell_1 \geq \ell_2 \geq \dots \geq \ell_N$. We compute the Lyapunov exponents using the standard dynamical algorithm based on QR-decomposition.^{55,56} In particular, simulations have been performed using the *DynamicalSystems.jl* Julia package⁵⁷ (see Appendix B for more details on numerical simulations).
- The fractal dimension of a chaotic attractor can be approximated using the Kaplan–Yorke formula,⁵⁸ given by

$$\mathcal{D}_{\text{KY}} = j + \frac{\sum_{i=1}^j \ell_i}{|\ell_{j+1}|}, \quad (\text{A3})$$

- where j is such that $\sum_{i=1}^j \ell_i \geq 0$ but $\sum_{i=1}^{j+1} \ell_i < 0$.
- Another measure of dynamical complexity is the Kolmogorov–Sinai dynamical entropy h_{KS} , which measures the growth rate of distinguishable trajectories in phase space.^{55,59} Following Pesin's formula, h_{KS} can be computed as the sum of all positive Lyapunov exponents,

$$h_{\text{KS}} = \sum_{i=1}^n \ell_i, \quad (\text{A4})$$

where n is such that $\ell_n \geq 0$ and $\ell_{n+1} < 0$.

APPENDIX B: NUMERICAL SIMULATIONS AND NUMERICAL CONTINUATION

The code used in this paper is openly available in Ref. 60 (also accessible through <https://github.com/pclus/KuramotoPopulationNetwork>). Simulations of the model and computation of Lyapunov exponents have been performed in Julia via the *DynamicalSystems.jl* package.⁵⁷ In particular, we have employed the Runge–Kutta 4 algorithm with a fixed time step of $dt = 10^{-2}$.

Simulations of the system employed an initial transient evolution of 6000 time units. This is a conservative transient time set to achieve a good convergence near the bifurcations, but for most parameter values shorter transients provide the same results. After this transient, we simulate both phase space and tangent space dynamics for the computation of the Lyapunov exponents. The tangent space is initially evolved for 200 time units, after which we start computing all the Lyapunov exponents for a total of 1000 time units. The QR decomposition for computation of the spectra is invoked at every time unit (i.e., $1/dt$ time steps). The computation of the Kaplan–Yorke formula requires a tolerance to discern zero and non-zero exponents, which we set to 10^{-4} .

The results depicted in Figs. 7(a2)–7(d2) require longer computation times due to the existence of the slow chaotic regime. In that case, the integration time step was chosen to be $dt = 10^{-1}$, the transient in tangent space consisted of 10^4 time units, and the Lyapunov exponents were computed for 3×10^4 time units with the QR decomposition at every 10 time units. Also in this case, we lowered the tolerance for the Kaplan–Yorke formula to 2×10^{-5} .

Simulations of the ring network for $\mu = 0.9$ were initialized at the antiphase state with an additional small random perturbation. This prevents the system from stalling into a long chaotic transient in the region where the antiphase state is stable. For all other

cases, since the antiphase state does not exist or is unstable, simulations were initialized at the homogeneous state with a random small perturbation.

The bifurcation diagrams of Fig. 3 were partially obtained with the numerical continuation software auto-07p.³⁹ In order to simplify the analysis, the two-population model with the connectivity matrix (16) was rewritten as a three-dimensional system in real space by considering the polar representation of the Kuramoto complex parameters $Z_1 = R_1 e^{i\Phi_1}$ and $Z_2 = R_2 e^{i\Phi_2}$ and defining a new variable $\Theta = \Phi_1 - \Phi_2$. Then, Eq. (3) reads

$$\begin{aligned}\dot{R}_1 &= -\Delta R_1 + K \left(\frac{1 - R_1^2}{2} \right) [\mu R_1 \cos(\alpha) + (1 - \mu) R_2 \cos(\Theta - \alpha)] \\ \dot{R}_2 &= -\Delta R_2 + K \left(\frac{1 - R_2^2}{2} \right) [\mu R_2 \cos(\alpha) + (1 - \mu) R_1 \cos(\Theta + \alpha)] \\ \dot{\Theta} &= K \left(\frac{1 + R_1^2}{2R_1} \right) [\mu R_1 \sin(\alpha) - (1 - \mu) R_2 \sin(\Theta - \alpha)] \\ &\quad - K \left(\frac{1 + R_2^2}{2R_2} \right) [\mu R_2 \sin(\alpha) + (1 - \mu) R_1 \sin(\Theta + \alpha)].\end{aligned}\quad (\text{B1})$$

A tutorial guide to obtain some of the bifurcations using the numerical continuation capabilities of auto-07p is openly available in the published repository.⁵⁰

APPENDIX C: PARAMETER REDUCTION

System (3) contains three parameters: Δ , K , and α . It is possible to rescale this system in order to reduce the parameter number to two. Some works^{10,12,13} consider systems in which time is rescaled as $\tilde{t} = Kt$ so that the coupling strength K can be removed from the equations or, equivalently, let it constant as $K = 1$. In this case, Eq. (3) reads

$$\frac{dZ_\sigma}{dt} = -DZ_\sigma + \frac{1}{2} \sum_{\kappa=1}^N c_{\sigma\kappa} (Z_\kappa e^{-i\alpha} - Z_\sigma^2 Z_\kappa^* e^{i\alpha}), \quad (\text{C1})$$

where $D = \Delta/K$ and $K > 0$.

Another option is to rescale time as $\tilde{t} = \Delta t$, such that (3) reads

$$\frac{dZ_\sigma}{d\tilde{t}} = -Z_\sigma + \frac{\tilde{K}}{2} \sum_{\kappa=1}^N c_{\sigma\kappa} (Z_\kappa e^{-i\alpha} - Z_\sigma^2 Z_\kappa^* e^{i\alpha}), \quad (\text{C2})$$

with $\tilde{K} = K/\Delta$ and $\Delta > 0$. This would be equivalent to let $\Delta = 1$ fixed in the equations.

In this work, we choose not to rescale any parameter in the system, so the analysis remains valid in the limit cases $\Delta = 0$ and $K = 0$. Nonetheless, we are mostly interested in the heterogeneous case ($\Delta > 0$); thus, we let $\Delta = 1$ without loss of generality. Therefore, in the two-population model, the equivalence between the formulation of previous studies^{10–13} and that given in Eq. (3) with $\Delta = 1$ is simply $D = 1/K$.

APPENDIX D: TRANSVERSE INSTABILITIES OF THE INCOHERENT STATE

Here study the transverse instabilities of the incoherent homogeneous state $Z_\sigma = 0$ for $\sigma = 1, \dots, N$. Our aim is to show that

transverse instabilities do not arise when this state is stable, i.e., when $0 < K \cos(\alpha) < 2\Delta$. Without loss of generality, we impose $\bar{\omega} = 0$. Then, by linearizing Eq. (3) around the incoherent solution ($Z_\sigma = 0$), we obtain

$$\dot{z}_\sigma = -\Delta z_\sigma + \frac{K}{2} \sum_{\kappa=1}^M c_{\sigma\kappa} z_\kappa e^{-i\alpha} = A^{(0)} z_\sigma + B^{(0)} \sum_{\kappa=1}^N c_{\sigma\kappa} z_\kappa, \quad (\text{D1})$$

where

$$A^{(0)} = \begin{pmatrix} -\Delta & 0 \\ 0 & -\Delta \end{pmatrix} \quad (\text{D2})$$

and

$$B^{(0)} = \frac{K}{2} \begin{pmatrix} \cos(\alpha) & \sin(\alpha) \\ -\sin(\alpha) & \cos(\alpha) \end{pmatrix}. \quad (\text{D3})$$

Following again the master stability formalism presented in Sec. III, the stability of this solution is controlled by the eigenvalues $\lambda_k^{(\pm)}$ of the matrices,

$$M_k^{(0)} = A^{(0)} + \Lambda_k B^{(0)} \quad \text{for } k = 1, \dots, N. \quad (\text{D4})$$

Now, instead of finding a general expression for the eigenvalues, it is enough to see that

$$\text{Tr}(M_k^{(0)}) = \lambda_k^{(+)} + \lambda_k^{(-)} = \Lambda_k K \cos(\alpha) - 2\Delta. \quad (\text{D5})$$

The incoherent solution $Z^{(0)}$ is stable within the homogeneous manifold Eq. (4) if and only if $K \cos(\alpha) < 2\Delta$. In this case, since $-1 \leq \Lambda_k \leq 1$ and $\Delta > 0$, we have that $\text{Tr}(M_k^{(0)}) < 0$. Therefore, transverse instabilities of the incoherent state may emerge only if this state is already unstable to the homogeneous perturbation.

APPENDIX E: TWISTED STATES IN RING NETWORKS

The ring topology given by Eq. (17) allows for the existence of twisted states. Twisted states are a particular case of traveling wave solution in which all populations share the same level of synchronization, $R_\sigma = \tilde{R}$, but with different collective phases Φ_σ . In particular, we are interested on studying solutions of the type

$$Z_\sigma = \tilde{R} e^{i(\tilde{\Omega}t + \beta\sigma)}, \quad (\text{E1})$$

where $\beta = 2\pi q/N$, with q being the winding number of the traveling wave. For $q = 0$, we recover the homogeneous solution studied in the paper, whereas for $q = N/2$, we obtain the antiphase state.

Inserting the expression in Eq. (E1) into the system Eq. (3), we obtain

$$\tilde{R} = \sqrt{1 - \frac{2\Delta}{K\Gamma \cos(\alpha)}}, \quad (\text{E2})$$

$$\tilde{\Omega} = \bar{\omega} - \tan(\alpha)[K\Gamma \cos(\alpha) - \Delta], \quad (\text{E3})$$

where $\Gamma = \mu + (1 - \mu) \cos(\beta)$. Notice that the existence region of these states is delimited by $K\Gamma \cos(\alpha) - 2\Delta = 0$.

We can perform linear stability analysis of these family of solutions following a similar reasoning as for the homogeneous state but with a few changes. Choosing $\bar{\omega} = \tan(\alpha)[K\Gamma \cos(\alpha) - \Delta]$ such

that $\tilde{\Omega} = 0$, the linear evolution of an arbitrary perturbation of a twisted state reads

$$\dot{z}_\sigma = \left(-\Delta + i\bar{\omega} - K\Gamma \tilde{R}^2 e^{i\alpha} \right) z_\sigma + \frac{K}{2} \sum_{\kappa=1}^M c_{\sigma\kappa} [z_\kappa e^{-i\alpha} - \tilde{R}^2 e^{i(2\beta\sigma+\alpha)} z_\kappa^*]. \quad (\text{E4})$$

Without loss of generality, we perform the change of variables $\zeta_\sigma = z_\sigma e^{-i\beta\sigma}$, thus

$$\begin{aligned} \dot{\zeta}_\sigma = & \left[-\Delta + i\bar{\omega} - K\Gamma \tilde{R}^2 e^{i\alpha} + \frac{K\mu}{2} e^{-i\alpha} \right] \zeta_\sigma - \frac{K\mu}{2} \tilde{R}^2 e^{i\alpha} \zeta_\sigma^* \\ & + \frac{1-\mu}{2} \left\{ \frac{1-\mu}{2} [e^{i(\beta-\alpha)} \zeta_{\sigma+1} - \tilde{R}^2 e^{-i(\beta-\alpha)} \zeta_{\sigma+1}^*] \right. \\ & \left. + \frac{1-\mu}{2} [e^{-i(\beta+\alpha)} \zeta_{\sigma-1} - \tilde{R}^2 e^{i(\beta+\alpha)} \zeta_{\sigma-1}^*] \right\}, \end{aligned} \quad (\text{E5})$$

where we have made explicit the coupling terms $c_{\sigma\kappa}$. As in the analysis of homogeneous states, we simplify the expressions writing the complex quantities in matricial form. Additionally, we include the coupling terms for the nearest neighbors as two new coupling matrices, $C^{(1)}$ and $C^{(2)}$ with elements given by

$$c_{\sigma\kappa}^{(1)} = \frac{1-\mu}{2} \delta_{\sigma,\kappa-1} \quad \text{and} \quad c_{\sigma\kappa}^{(2)} = \frac{1-\mu}{2} \delta_{\sigma,\kappa+1}, \quad (\text{E6})$$

where $\delta_{\sigma,\kappa}$ is the Kronecker delta. Then, the evolution of the perturbation reads

$$\dot{\zeta}_\sigma = \tilde{A} \zeta_\sigma + \sum_{\kappa=1}^N (c_{\sigma\kappa}^{(1)} \tilde{B}^{(1)} + c_{\sigma\kappa}^{(2)} \tilde{B}^{(2)}) \zeta_\kappa, \quad (\text{E7})$$

where

$$\tilde{A} = \begin{pmatrix} \Delta \left(1 + \frac{\mu}{\Gamma}\right) - K\Gamma \cos(\alpha) & \Delta \tan(\alpha) \left(\frac{\mu}{\Gamma} - 1\right) \\ \Delta \tan(\alpha) \left(\frac{\mu}{\Gamma} + 1\right) - \mu K \sin(\alpha) & \Delta \left(1 - \frac{\mu}{\Gamma}\right) + (\mu - \Gamma) K \cos(\alpha) \end{pmatrix}, \quad (\text{E8})$$

$$\tilde{B}^{(1)} = \begin{pmatrix} \frac{\cos(\beta - \alpha)\Delta}{\cos(\alpha)\Gamma} & -\frac{\sin(\beta - \alpha)\Delta}{\cos(\alpha)\Gamma} \\ \sin(\beta - \alpha) \left(K - \frac{\Delta}{\Gamma \cos(\alpha)}\right) & \cos(\beta - \alpha) \left(K - \frac{\Delta}{\Gamma \cos(\alpha)}\right) \end{pmatrix}, \quad (\text{E9})$$

and

$$\tilde{B}^{(2)} = \begin{pmatrix} \frac{\cos(\beta + \alpha)\Delta}{\cos(\alpha)\Gamma} & -\frac{\sin(\beta + \alpha)\Delta}{\cos(\alpha)\Gamma} \\ \sin(\beta + \alpha) \left(K - \frac{\Delta}{\Gamma \cos(\alpha)}\right) & \cos(\beta + \alpha) \left(K - \frac{\Delta}{\Gamma \cos(\alpha)}\right) \end{pmatrix}. \quad (\text{E10})$$

Now, notice that matrices $C^{(1)}$ and $C^{(2)}$ are circulant, thus sharing the same eigenvectors. Therefore, we can write the perturbation ζ_σ in the basis provided by these eigenvectors and, following the same arguments as for the homogeneous state, we finally obtain that the eigenvalues controlling the stability of the twisted state with parameter β correspond to the $2N$ eigenvalues of the family of matrices,

$$\tilde{A} + \tilde{\Lambda}_k^{(1)} \tilde{B}^{(1)} + \Lambda_k^{(2)} \tilde{B}^{(2)}, \quad (\text{E11})$$

for $k = 1, \dots, N$, where

$$\Lambda_k^{(1)} = \frac{1-\mu}{2} e^{-i\frac{2\pi k}{N}} \quad \text{and} \quad \Lambda_k^{(2)} = \frac{1-\mu}{2} e^{i\frac{2\pi k}{N}} \quad (\text{E12})$$

are the eigenvalues of $C^{(1)}$ and $C^{(2)}$, respectively.

[Figures 10\(a\)](#) and [10\(b\)](#) show a bifurcation diagram of twisted states for ring networks composed of $N = 24$ and $N = 128$ populations, respectively. Different colored lines indicate the stability boundaries of twisted states with winding number q . The gray-shaded area shows the parameter region where no twisted state is stable. In both figures, the homogeneous solution ($q = 0$) is the state

with a larger stability region. Most other twisted states become stable only for high values of K , for which there exist different forms of multistability between these planar wave solutions. The exceptions are the antiphase state ($q = N/2$) and the three-cluster state in [Fig. 10\(b\)](#) ($q = N/3 = 8$), which are stable in regions where no other twisted states exhibit stability. [Figures 11\(a\)](#) and [11\(b\)](#) show two examples of twisted dynamics for $N = 24$ with winding numbers $q = 1$ [panel (a)] and $q = 3$ [panel (b)].

APPENDIX F: ANTI-PHASE STATES IN RING NETWORKS

Here, we provide the stability analysis of antiphase states in topologies given by either Eqs. [\(16\)](#) or [\(17\)](#) with an even number of populations N . Antiphase states are a particular case of twisted states with winding number $q = N/2$ ($\beta = \pi$). Thus, the analysis provided in [Appendix E](#) also applies here. Nonetheless, for this particular case, we can provide a simpler analysis in close analogy to that performed

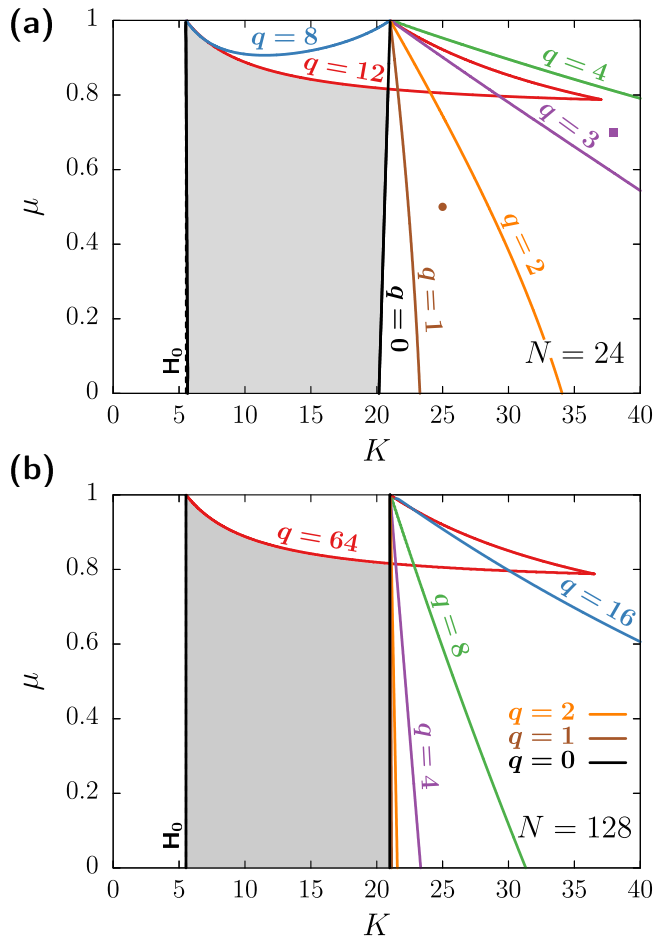


FIG. 10. Bifurcation diagrams for twisted states in ring networks with $N = 24$ [panel (a)] and $N = 128$ [panel (b)]. Colored curves show the stability boundaries of twisted states with different winding number q , with labels located in the region of stability. The gray-shaded region indicates the region where no twisted state is stable. The vertical dashed line indicates the Kuramoto synchronization transition H_0 . In panel (b), the boundary of the solution corresponding to $q = 1$ (brown curve) is barely visible, as it is almost identical to that of $q = 0$ (black curve). Brown circle and purple square in panel (a) indicate the parameters corresponding to the simulations depicted in Fig. 11.

in Sec. III. Antiphase states are solutions of Eq. (3) given by

$$Z_\sigma = \begin{cases} \hat{R} e^{i\hat{\Omega}t} & \text{if } \sigma \text{ is even} \\ \hat{R} e^{i(\hat{\Omega}t+\pi)} & \text{if } \sigma \text{ is odd.} \end{cases} \quad (\text{F1})$$

Inserting these expressions into Eq. (3) and using the corresponding expression of $c_{\sigma\kappa}$, we obtain that

$$\hat{R} = \sqrt{1 - \frac{2\Delta}{K(2\mu - 1)\cos(\alpha)}} \quad \text{and} \quad (\text{F2})$$

$$\hat{\Omega} = \bar{\omega} - \tan(\alpha)[K(2\mu - 1)\cos(\alpha) - \Delta].$$

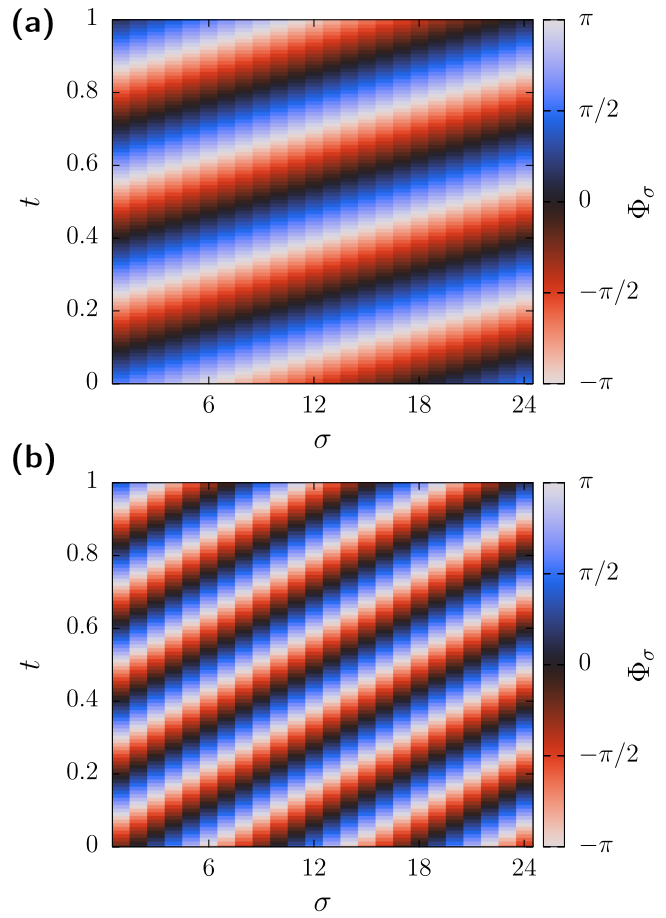


FIG. 11. Simulations of twisted states in the ring model with $N = 24$. (a) Twisted state with $q = 1$, corresponding to $K = 25$ and $\mu = 0.5$ [see brown circle in Fig. 10(a)]. (b) Twisted state with $q = 3$, corresponding to $K = 38$ and $\mu = 0.7$ [see purple square in Fig. 10(a)]. In both cases, only the collective phase Φ_σ is shown, as R_σ is homogeneous. Simulations have been initialized close to the corresponding twisted state, with $\bar{\omega} = 0$ for visualization.

By linearizing (3) around this solution, we obtain

$$\dot{z}_\sigma = \left(-\Delta + i\bar{\omega} - K(2\mu - 1)\hat{R}^2 e^{i\alpha} \right) z_\sigma + \frac{K}{2} \sum_{\kappa=1}^M c_{\sigma\kappa} \left(z_\kappa e^{-i\alpha} - \hat{R}^2 z_\kappa^* e^{i\alpha} \right). \quad (\text{F3})$$

By choosing $\bar{\omega} = \tan(\alpha)[K(2\mu - 1)\cos(\alpha) - \Delta]$ and replacing the expression of \hat{R} from Eq. (F2), we obtain

$$\dot{z}_\sigma = \hat{A} z_\sigma + \hat{B} \sum_{\kappa=1}^N c_{\sigma\kappa} z_\kappa, \quad (\text{F4})$$

where

$$\hat{A} = \begin{pmatrix} \Delta - K\cos(\alpha)(2\mu - 1) & -\Delta \tan(\alpha) \\ \Delta \tan(\alpha) & \Delta - K\cos(\alpha)(2\mu - 1) \end{pmatrix} \quad (\text{F5})$$

and

$$\hat{B} = \begin{pmatrix} \frac{\Delta}{2\mu-1} & \frac{\Delta}{2\mu-1} \tan(\alpha) \\ -K \sin(\alpha) + \frac{\Delta}{2\mu-1} \tan(\alpha) & K \cos(\alpha) - \frac{\Delta}{2\mu-1} \end{pmatrix}. \quad (\text{F6})$$

Analogously to the stability of the homogeneous states shown in Sec. III, we apply the MSF formalism based on decomposing a perturbation on the basis of the eigenvectors of the connectivity matrix C . As a result, we obtain that the stability of the antiphase state is given by the eigenvalues of the $N 2 \times 2$ matrices,

$$\hat{M}_k = \hat{A} + \Lambda_k \hat{B} \quad \text{for } k = 1, \dots, N, \quad (\text{F7})$$

where Λ_k are obtained from Eq. (18). The explicit expression of the system eigenvalues reads

$$\begin{aligned} \hat{\lambda}_k^{(\pm)} = & \Delta + K \cos(\alpha) \left(\frac{\Lambda_k}{2} + 1 - 2\mu \right) \\ & \pm \left\{ \frac{K^2 \Lambda_k^2 \cos^2(\alpha)}{4} \right. \\ & + \frac{K \Lambda_k \Delta \cos(\alpha)}{2\mu-1} [\tan^2(\alpha)(2\mu-1-\Lambda_k) - \Lambda_k] \\ & \left. + \frac{\Delta^2}{(2\mu-1)^2} [(\Lambda_k^2 - (2\mu-1)^2) \tan^2(\alpha) + \Lambda_k^2] \right\}^{1/2}. \end{aligned} \quad (\text{F8})$$

From this expression, we shall highlight several aspects:

- As in the homogeneous state, the antiphase state is a periodic solution in a co-rotating frame. Therefore, at least one of the eigenvalues has to be 0. This corresponds to $\Lambda_N = 2\mu - 1$, as the associated eigenvector indicates perturbations acting opposite on each node consecutively, i.e., from Eq. (19),

$$\Psi_j^{(N)} = \begin{cases} \frac{1}{\sqrt{N}} & \text{if } j \text{ is odd,} \\ \frac{-1}{\sqrt{N}} & \text{if } j \text{ is even.} \end{cases} \quad (\text{F9})$$

- Taking into account the previous point, for $N = 2$, the stability of the antiphase solution is controlled by the eigenvalue associated to $k = 1$. Substituting, thus, $\Lambda_1 = 1$ in Eq. (F8) and solving for $\lambda_1^{(\pm)} = 0$, we obtain the bifurcations from the antiphase state in the two-population model. This eigenvalue can be zero through a pair of complex conjugates or a single real eigenvalue, defining thus the subcritical Hopf (H-) and the pitchfork (PF-) bifurcations displayed in Fig. 3.
- For $N > 2$, other eigenvalues rather than Λ_1 can lead to instabilities of the antiphase state. This is the case of Fig. 5(a), in which the left branch of the instability is always given by Λ_1 , but the right branch corresponds to other modes depending on N .

REFERENCES

- Y. Kuramoto and D. Battogtokh, "Coexistence of coherence and incoherence in nonlocally coupled phase oscillators," *Nonlinear Phenom. Complex Syst.* **5**, 380 (2002).
- D. M. Abrams and S. H. Strogatz, "Chimera states for coupled oscillators," *Phys. Rev. Lett.* **93**, 174102 (2004).
- F. Parastesh, S. Jafari, H. Azarnoush, Z. Shahriari, Z. Wang, S. Boccaletti, and M. Perc, "Chimeras," *Phys. Rep.* **898**, 1–114 (2021).
- S. W. Haugland, "The changing notion of chimera states, a critical review," *J. Phys.: Complexity* **2**, 032001 (2021).
- H. Sakaguchi and Y. Kuramoto, "A soluble active rotator model showing phase transitions via mutual entertainment," *Prog. Theor. Phys.* **76**, 576–581 (1986).
- E. Ott and T. M. Antonsen, "Low dimensional behavior of large systems of globally coupled oscillators," *Chaos* **18**, 037113 (2008).
- C. Bick, M. Goodfellow, C. R. Laing, and E. A. Martens, "Understanding the dynamics of biological and neural oscillator networks through exact mean-field reductions: A review," *J. Math. Neurosci.* **10**, 9 (2020).
- See also the Watanabe-Strogatz theory,⁶¹ which provides a complete description for the homogeneous case. For a comprehensive general theory that includes and relates Watanabe-Strogatz and Ott-Antonsen frameworks, see Ref. 32.
- D. M. Abrams, R. Mirollo, S. H. Strogatz, and D. A. Wiley, "Solvable model for chimera states of coupled oscillators," *Phys. Rev. Lett.* **101**, 084103 (2008).
- C. R. Laing, "Chimera states in heterogeneous networks," *Chaos* **19**, 013113 (2009).
- C. R. Laing, "Disorder-induced dynamics in a pair of coupled heterogeneous phase oscillator networks," *Chaos* **22**, 043104 (2012).
- T. Kotwal, X. Jiang, and D. M. Abrams, "Connecting the kuramoto model and the chimera state," *Phys. Rev. Lett.* **119**, 264101 (2017).
- S. Guo, M. Yang, W. Han, and J. Yang, "Dynamics in two interacting subpopulations of nonidentical phase oscillators," *Phys. Rev. E* **103**, 052208 (2021).
- For studies of non-identical populations (i.e., ensembles governed by different parameter values), see Refs. 62–64.
- E. A. Martens, "Chimeras in a network of three oscillator populations with varying network topology," *Chaos* **20**, 043122 (2010).
- E. A. Martens, "Bistable chimera attractors on a triangular network of oscillator populations," *Phys. Rev. E* **82**, 016216 (2010).
- S. Lee and K. Krischer, "Chaotic chimera attractors in a triangular network of identical oscillators," *Phys. Rev. E* **107**, 054205 (2023).
- S. Lee and K. Krischer, "Heteroclinic switching between chimeras in a ring of six oscillator populations," *Chaos* **33**, 063120 (2023).
- C. R. Laing, "Chimeras on a ring of oscillator populations," *Chaos* **33**, 013121 (2023).
- L. M. Pecora and T. L. Carroll, "Master stability functions for synchronized coupled systems," *Phys. Rev. Lett.* **80**, 2109–2112 (1998).
- D. Ruelle, "Large volume limit of the distribution of characteristic exponents in turbulence," *Commun. Math. Phys.* **87**, 287–302 (1982).
- P. Manneville, "Lyapounov exponents for the kuramoto-sivashinsky model," in *Macroscopic Modelling of Turbulent Flows: Proceedings of a Workshop Held at INRIA, Sophia-Antipolis, France, December 10–14, 1984* (Springer, 1985), pp. 319–326.
- R. Livi, A. Politi, and S. Ruffo, "Distribution of characteristic exponents in the thermodynamic limit," *J. Phys. A: Math. Gen.* **19**, 2033–2040 (1986).
- L. Keefe, "Properties of Ginzburg-Landau attractors associated with their Lyapunov vectors and spectra," *Phys. Lett. A* **140**, 317–322 (1989).
- C. S. O'Hern, D. A. Egolf, and H. S. Greenside, "Lyapunov spectral analysis of a nonequilibrium Ising-like transition," *Phys. Rev. E* **53**, 3374–3386 (1996).
- D. A. Egolf, I. V. Melnikov, W. Pesch, and R. E. Ecke, "Mechanisms of extensive spatiotemporal chaos in Rayleigh-Bénard convection," *Nature* **404**, 733–736 (2000).
- H.-W. Xi, R. Toral, J. D. Gunton, and M. I. Tribelsky, "Extensive chaos in the nikolaevskii model," *Phys. Rev. E* **62**, R17–R20 (2000).
- M. R. Paul, M. I. Einarsson, P. F. Fischer, and M. C. Cross, "Extensive chaos in Rayleigh-Bénard convection," *Phys. Rev. E* **75**, 045203 (2007).
- M. Monteforte and F. Wolf, "Dynamical entropy production in spiking neuron networks in the balanced state," *Phys. Rev. Lett.* **105**, 268104 (2010).
- A. Palmigiano, R. Engelken, and F. Wolf, "Boosting of neural circuit chaos at the onset of collective oscillations," *eLife* **12**, RP0378 (2023).
- K. A. Takeuchi, H. Chaté, F. Ginelli, A. Politi, and A. Torcini, "Extensive and subextensive chaos in globally coupled dynamical systems," *Phys. Rev. Lett.* **107**, 124101 (2011).

- ³²R. Cestnik and A. Pikovsky, "Exact finite-dimensional reduction for a population of noisy oscillators and its link to Ott-Antonsen and Watanabe-Strogatz theories," *Chaos* **32**, 113126 (2022).
- ³³See Refs. [65–67](#) for introductory reviews on the MSF formalism. Although most studies on the MSF rely on diffusive coupling or variations of it via a Laplacian matrix (see, e.g., Ref. [68](#)), the method is applicable to any setup having a homogeneous solution (see, e.g., Ref. [53](#)).
- ³⁴J. Wilkinson, *The Algebraic Eigenvalue Problem*, Monographs on Numerical Analysis (Clarendon Press, 1967).
- ³⁵The homogeneous synchronized solution emerges only for $\Delta - K \cos(\alpha)/2 < 0$, which leads to $\Delta + K \cos(\alpha) (\frac{\Lambda}{2} - 1) < 0$ in Eq. [\(14\)](#) (since $\Delta \geq 0$ and $-1 \leq \Lambda \leq 1$). Therefore, eigenvalues with positive real part in Eq. [\(14\)](#) always correspond to real eigenvalues. Complex conjugate eigenvalues might exist, but they correspond to stable directions.
- ³⁶Y. Kuramoto, *Chemical Oscillations, Waves and Turbulence* (Springer, Berlin, 1984).
- ³⁷M. Wolfrum, S. V. Gurevich, and O. E. Omel'chenko, "Turbulence in the Ott-Antonsen equation for arrays of coupled phase oscillators," *Nonlinearity* **29**, 257–270 (2016).
- ³⁸In this case, the bifurcation boundary is given by $K \cos^3(\alpha) = \Delta$, which can be obtained by deriving Eq. [\(14\)](#) with respect to Λ_k and then solving $\frac{d}{d\Lambda_k} \lambda^{(+)}|_{\Lambda_k=1} = 0$.
- ³⁹E. J. Doedel, A. R. Champneys, F. Deroche, T. F. Fairgrieve, Y. A. Kuznetsov, B. Oldeman, R. Paffenroth, B. Sandstede, X. Wang, and C. Zhang, "Auto-07p: Continuation and bifurcation software for ordinary differential equations" (2007).
- ⁴⁰For $\alpha = 1.2$, we did not find the chaotic state unveiled in Ref. [11](#), but it can be attained, for instance, at $(K, \mu, \alpha, \Delta) = (20, 0.9, 1.25, 1)$.
- ⁴¹J. M. Lopez and F. Marques, "Dynamics of three-tori in a periodically forced navier-stokes flow," *Phys. Rev. Lett.* **85**, 972–975 (2000).
- ⁴²D. Pazó and V. Pérez-Muñozuri, "Onset of wave fronts in a discrete bistable medium," *Phys. Rev. E* **64**, 065203 (2001).
- ⁴³O. E. Omel'chenko, M. Wolfrum, and C. R. Laing, "Partially coherent twisted states in arrays of coupled phase oscillators," *Chaos* **24**, 023102 (2014).
- ⁴⁴We also performed simulations with adiabatic increase and decrease of K in order to test for potential bistability between the fast and slow chaotic states. The outcome consistently showed the disappearance of the faster dynamics around $K \approx 15.5$.
- ⁴⁵C. R. Laing, "The dynamics of chimera states in heterogeneous Kuramoto networks," *Physica D* **238**, 1569–1588 (2009).
- ⁴⁶T. B. Benjamin and J. E. Feir, "The disintegration of wave trains on deep water part 1. Theory," *J. Fluid Mech.* **27**, 417–430 (1967).
- ⁴⁷M. Bolotov, L. Smirnov, G. Osipov, and A. Pikovsky, "Simple and complex chimera states in a nonlinearly coupled oscillatory medium," *Chaos* **28**, 045101 (2018).
- ⁴⁸M. I. Bolotov, L. A. Smirnov, E. S. Bubnova, G. V. Osipov, and A. S. Pikovsky, "Spatiotemporal regimes in the Kuramoto-Battogtokh system of nonidentical oscillators," *J. Exp. Theor. Phys.* **132**, 127–147 (2021).
- ⁴⁹G. Filatrella, A. H. Nielsen, and N. F. Pedersen, "Analysis of a power grid using a Kuramoto-like model," *Eur. Phys. J. B* **61**, 485–491 (2008).
- ⁵⁰S. H. Strogatz, "Human sleep and circadian rhythms: A simple model based on two coupled oscillators," *J. Math. Biol.* **25**, 327–347 (1987).
- ⁵¹J. Liu, R. Martinez-Corral, A. Prindle, D. Yeon, D. Lee, J. Larkin, M. Gabaldón-Sagarra, J. García-Ojalvo, and G. M. Suel, "Coupling between distant biofilms and emergence of nutrient time-sharing," *Science* **356**, 638–642 (2017).
- ⁵²P. Clusella, B. Pietras, and E. Montbrió, "Kuramoto model for populations of quadratic integrate-and-fire neurons with chemical and electrical coupling," *Chaos* **32**, 013105 (2022).
- ⁵³P. Clusella, G. Deco, M. L. Kringselbach, G. Ruffini, and J. García-Ojalvo, "Complex spatiotemporal oscillations emerge from transverse instabilities in large-scale brain networks," *PLoS Comput. Biol.* **19**, e1010781 (2023).
- ⁵⁴A. Politi, "Lyapunov exponent," *Scholarpedia* **8**, 2722 (2013).
- ⁵⁵A. Pikovsky and A. Politi, *Lyapunov Exponents: A Tool to Explore Complex Dynamics* (Cambridge University Press, Cambridge, 2016).
- ⁵⁶G. Benettin, L. Galgani, A. Giorgilli, and J.-M. Strelcyn, "Lyapunov characteristic exponents for smooth dynamical systems and for hamiltonian systems; a method for computing all of them. Part 2: Numerical application," *Meccanica* **15**, 21–30 (1980).
- ⁵⁷G. Datseris, "Dynamicalsystems.jl: A julia software library for chaos and nonlinear dynamics," *J. Open Source Software* **3**, 598 (2018).
- ⁵⁸J. L. Kaplan and J. A. Yorke, "Chaotic behavior of multidimensional difference equations," in *Functional Differential Equations and Approximation of Fixed Points*, edited by H.-O. Peitgen and H.-O. Walther (Springer, Berlin, Heidelberg, 1979), pp. 204–227.
- ⁵⁹Y. Sinai, "Kolmogorov-Sinai entropy," *Scholarpedia* **4**, 2034 (2009).
- ⁶⁰P. Clusella (2024). "plus/KuramotoPopulationNetwork: First release," Zenodo. <https://doi.org/10.5281/zenodo.13912549>.
- ⁶¹X.-J. Wang and G. Buzsáki, "Gamma oscillation by synaptic inhibition in a hippocampal interneuronal network model," *J. Neurosci.* **16**, 6402–6413 (1996).
- ⁶²E. Montbrió, J. Kurths, and B. Blasius, "Synchronization of two interacting populations of oscillators," *Phys. Rev. E* **70**, 056125 (2004).
- ⁶³E. A. Martens, C. Bick, and M. J. Panaggio, "Chimera states in two populations with heterogeneous phase-lag," *Chaos* **26**, 094819 (2016).
- ⁶⁴C.-U. Choe, J.-S. Ri, and R.-S. Kim, "Incoherent chimera and glassy states in coupled oscillators with frustrated interactions," *Phys. Rev. E* **94**, 032205 (2016).
- ⁶⁵A. Arenas, A. Díaz-Guilera, J. Kurths, Y. Moreno, and C. Zhou, "Synchronization in complex networks," *Phys. Rep.* **469**, 93–153 (2008).
- ⁶⁶M. Porter, and J. Gleeson, *Dynamical Systems on Networks: A Tutorial, Frontiers in Applied Dynamical Systems: Reviews and Tutorials* (Springer International Publishing, 2016).
- ⁶⁷P. Ashwin, S. Coombes, and R. Nicks, "Mathematical frameworks for oscillatory network dynamics in neuroscience," *J. Math. Neurosci.* **6**, 2 (2016).
- ⁶⁸H. Nakao, "Complex Ginzburg-Landau equation on networks and its nonuniform dynamics," *Eur. Phys. J. Spec. Top.* **223**, 2411–2421 (2014).